



저작자표시-비영리-변경금지 2.0 대한민국

이용자는 아래의 조건을 따르는 경우에 한하여 자유롭게

- 이 저작물을 복제, 배포, 전송, 전시, 공연 및 방송할 수 있습니다.

다음과 같은 조건을 따라야 합니다:



저작자표시. 귀하는 원저작자를 표시하여야 합니다.



비영리. 귀하는 이 저작물을 영리 목적으로 이용할 수 없습니다.



변경금지. 귀하는 이 저작물을 개작, 변형 또는 가공할 수 없습니다.

- 귀하는, 이 저작물의 재이용이나 배포의 경우, 이 저작물에 적용된 이용허락조건을 명확하게 나타내어야 합니다.
- 저작권자로부터 별도의 허가를 받으면 이러한 조건들은 적용되지 않습니다.

저작권법에 따른 이용자의 권리는 위의 내용에 의하여 영향을 받지 않습니다.

이것은 [이용허락규약\(Legal Code\)](#)을 이해하기 쉽게 요약한 것입니다.

[Disclaimer](#)

Master of Science

**고효율 호이겐스 단위 셀을 이용한
빔포밍 투과형 메타표면 설계**

**Beamforming Transmission Metasurface Design
Using High-Efficiency Huygens' Unit Cells**

The Graduate School
Of the University of Ulsan
School of Electrical, Electronics and Computer Engineering

KD M RAZIUL ISLAM

**Beamforming Transmission Metasurface Design
Using High-Efficiency Huygens' Unit Cells**

Supervisor: Prof. Sangjo Choi

A Master's Thesis

Submitted to
the Graduate School of the University of Ulsan
in partial fulfillment of the requirements
for the degree of

Master of Science

by

KD M RAZIUL ISLAM

School of Electrical, Electronics and Computer Engineering
Ulsan, Republic of Korea

July 2021.

Beamforming Transmission Metasurface Design Using High-Efficiency Huygens' Unit Cells

This certifies that the Master's Thesis
of KD M RAZIUL ISLAM is approved.



Committee Chair, Prof. Hyung-Yun Kong



Committee Member, Prof. Jiho Song



Committee Member, Prof. Sangjo Choi

Department of Electrical, Electronics and Computer Engineering

Ulsan, Republic of Korea

July, 2021

ACKNOWLEDGEMENT

All praise and thanks belong to almighty ALLAH (SWT) who is the Lord of the universe.

I would like to express my sincere gratitude to my advisor Prof. Sangjo Choi of the School of Electrical, Electronics and Computer Engineering at the University of Ulsan for his supervision, advice, continuous support, and constant encouragement throughout my M.Sc. study and related research. His patience, motivation, immense knowledge, and continuous guidance helped to conduct my research and writing of this thesis. Besides my advisors, I am gratefully indebted to my other thesis committee members: Prof. Hyung-Yun Kong, Prof. Jiho Song, for their efforts to go through my thesis, insightful comments, and suggestions.

I would like to thank my lab mates Nasim Al Islam, Md Khoirul Anam, MD. Nazim Uddin and Sang Min, in the Electromagnetics System and Physics Lab for their friendship and support. I am very much grateful to the University of Ulsan for giving me such a wonderful research environment and financial support. My special thanks go to Brain Korea 21Plus Program for its contribution and financial support during my study.

I would like to express my heartiest thanks to Md Junayed Hasan, Md Jonaet Ansari, Md Niaz Morshedul Haque, Jaber AL Hossain, Md Maruf Mridha, Surajit Chakraborty for their love, respect, and support.

Finally, I am ever grateful to my parents KD M Nurul Islam and Afraza Begum for raising me and helping me to achieve all that I have in my life. I am also grateful to my wife Nushrat Afrose for her support and all the sacrifices, she has made, for my achievement. At last, I want to dedicate my thesis to all my family members who are the strength of my whole life.

KD M RAZIUL ISLAM

July, 2021

University of Ulsan

ABSTRACT

Metamaterials are substances with subwavelength structures that are engineered to have specific electromagnetic properties. The metamaterials show significant control on the properties of constituent materials and thus introduce numerous physical phenomena. However, metamaterials are deemed as less attractive due to their excessive losses, bulk size, and fabrication difficulty. These limitations have led to flourishing two-dimensional metamaterials, which are known as metasurfaces. Metasurfaces can bring medium discontinuities to the wavefronts of electromagnetic waves. As a result, it enables the tailoring of electromagnetic fields across a subwavelength scale.

The building blocks of metasurfaces are polarizable particles, which support strong current near resonance and control polarization and wavefront. This surface can be made as either reflective or transmissive surfaces. In this thesis, concentration is given on high-efficiency transmission metasurface unit cells based on surface electric and magnetic impedances derived from Huygens' Principle. However, unit cells for low transmission loss (< 1 dB) over a wide transmission phase range require at least three metallic layers, which complicates the unit cell design process. This work introduces high-efficiency Huygens' metasurface unit cell topologies in double-layer FR4 printed circuit board (PCB) by implementing surface electric and magnetic current using the top and bottom metallic patterns and via drills. Eleven unit cells were optimized for wide phase coverage (-150° to 150°) with a low average transmission loss of -0.82 dB at 10 GHz. Then, the high-efficiency of the designed unit cells has been demonstrated by designing and fabricating two focusing lenses with dimensions of near 150×150 mm ($5\lambda \times 5\lambda$) to focus a spherical beam radiated from short focal distances ($f = 100$ and 60 mm). The fabricated focusing lens showed 12.87 and 13.58 dB focusing gain for $f = 100$ and 60 mm at 10 GHz, respectively, with a 1 dB fractional gain bandwidth of near 13%.

Next, as an extension of the above work, reconfigurable/tunable unit cells based on the highly efficient unit structure have been constructed. In this extended work, recent development in the area of tunable metasurface designs has been highlighted. The surface reconfigurability in real-time has been realized by many tunable components (MEMS, Vanadium Dioxide, Graphene, Liquid Crystal, GaAs switch, and Schottky diode). However, the addition or realization of these

components makes the structure bulky and thus hinders the construction of a compact device. As an alternative, we used PIN (positive-intrinsic-negative) and varactor diodes combined with unit cells structure to make the unit cell less bulky, fabrication friendly, and highly transmissive.

TABLE OF CONTENTS

ACKNOWLEDGEMENT.....	1
ABSTRACT.....	2
TABLE OF CONTENTS.....	3
LIST OF FIGURES.....	4
LIST OF TABLES.....	7
CHAPTER 1: INTRODUCTION.....	7
1.1 Motivation and goal.....	7
1.2 Thesis Organization.....	8
CHAPTER 2: METAMATERIAL AND METASURFACE FUNDAMENTALS AND APPLICATIONS.....	9
2.1 The Metamaterial.....	10
2.2 The Metasurface and Application	10
2.2.1 Application Of Metasurface.....	11
2.3 The Huygens’ Metasurface.....	12
2.4 Theoretical Background of Huygens’ Metasurface.....	13
2.5 Generalized Sheet Transition Condition (GSTC).....	17
2.6 Literature Review On GSTC.....	18
CHAPTER 3: FOCUSING LENS WITH HIGH EFFICIENT HUYGENS’ METASURFACE UNIT CELLS.....	20
3.1 Literature Review on Huygens metasurface.....	20
3.1.1 Generalized Laws of Reflection and Transmission.....	20
3.1.2 Two-Layer Structures on printed circuit board (PCB).....	21
3.1.3 Three-Layer structures.....	23

3.1.4	This Work.....	23
3.2	Huygens' Metasurface Unit Cell Design.....	24
3.2.1	Unit Cell Design Method.....	24
3.2.2	Unit Cell Dimension.....	25
3.2.3	Unit Cell Topology Design and Analysis.....	26
3.3	Focusing Lens Design.....	35
3.3.1	Distance to Phase Relationship.....	35
3.3.2	Simulation Setup.....	37
3.4	Fabrication and Measurement.....	37
3.4.1	Measurement Setup.....	38
3.4.2	Simulation and Measured Result.....	39
3.4.3	Fractional Bandwidth Calculation.....	40
3.5	Discussion.....	42
CHAPTER 4: RECONFIGURABLE INTELLIGENT SURFACE DESIGN FOR BEAM STEERING		44
4.1	Reconfigurable Metasurface State of The Art.....	44
4.2	Problem Statement.....	46
4.3	Unit Cell Design Process.....	46
4.4	Lens Design and Expected Output.....	48
CHAPTER 5: CONCLUSION AND FUTURE WORK.....		49
5.1	Conclusion.....	49
5.2	Proposal for future works.....	50
	References.....	50

LIST OF FIGURES

Figure 2.1	Examples of metasurface applications [24].....	11
Figure 2.2	(a) - The Huygens-Fresnel theory is shown in this diagram, which depicts the incremental movement of a plane wave through secondary wave excitation. (b) - The Huygens-Fresnel principle is used to explain the event of refraction. (c) – Concept of Huygens' metasurfaces is depicted.....	13
Figure 2.3	Oblique incident of a plane wave at the boundary of two bulk mediums.....	15

Figure 2.4	Huygens metasurface with surface current (J_s , M_s) orthogonal at the interface. This current produce transmitted (E_2 , H_2) and reflected field from incident field. E_1 , H_1 are the combination of incident and reflected field. (n) is normal to the surface[43]..	16
Figure 3.11	Sketch of generalize Snell's law of refraction. The phase shifts are ϕ and $\phi + d\phi$ where blue and red paths crossed the boundary [56].....	21
Figure 3.12	(a) Fabricated Huygens Surface. (b) Top view which provides electric polarization current (c) Bottom structure for magnetic polarization current [57].....	22
Figure 3.13	(a) Transmit Unit cell of two-layer. (b) S_{21} Parameters of the Unit cell. [89].....	22
Figure 3.14	(a) Top and side view of two-layer unit cell with via. (b) Transmission performance of unit cell. [90].....	22
Figure 3.15	Dog bones and loaded dipole structure of three-layer. [97].....	23
Figure 3.16	Transmission phases versus the imaginary part of the normalized surface electric admittance $\text{Im}\{Y_{es}\eta_0\}$ and the normalized surface magnetic impedance $\text{Im}\{Z_{ms} / \eta_0\}$	25
Figure 3.17	Transmittance along the frequency from different unit cell lengths.....	26
Figure 3.18	Electric and magnetic dipole in topology 1 from the (a) side-side view and (b) top view.....	27
Figure 3.19	(a) Y_{es} and Z_{ms} values of the unit cell according to frequency for a transmission phase of -150° . (b) The y component of the electric field E_y . (c) The x component of the magnetic field H_x along the x-y plane in the middle of the unit cell at 10 GHz.....	28
Figure 3.2	(a) Y_{es} and Z_{ms} values of the unit cell along frequency for a transmission phase of $+150^\circ$. (b) The y component of the electric field E_y . (c) The x component of the magnetic field H_x along the x-y plane in the middle of the unit cell at 10 GHz.....	29
Figure 3.21	(a) Y_{es} and Z_{ms} values of the unit cell according to frequency for a transmission phase of $+120^\circ$. (b) The y component of the electric field E_y . (c) The x component of the magnetic field H_x along the x-y plane in the middle of the unit cell at 10GHz.	30
Figure 3.22	(a) Y_{es} and Z_{ms} values of the unit cell according to frequency for transmission phases of -150° and -120° . (b) The y component of the electric field E_y for the transmission phase of -120° . (c) The x component of the magnetic field H_x for -120° along the x-y plane in the middle of the unit cell at 10 GHz.....	31
Figure 3.23	Electric and magnetic dipoles in the topology 2 structure from the (a) side-side view and (b) top view. (c) Y_{es} and Z_{ms} values of the unit cell according to frequency for a transmission phase of -90° . (d) The y component of the electric field E_y . (e) The x component of the magnetic field H_x along the x-y plane in the middle of the unit cell at 10 GHz.....	32

Figure 3.24	Electric and magnetic dipoles in the topology 3 structure from the (a) side–side view and (b) top view.....	34
Figure 3.25	Y_{es} and Z_{ms} values of the unit cell according to frequency for transmission phases of (a) -60° and (b) -30° . The y component of the electric field E_y for transmission phases of (c) -60° and (d) -30° . The x component of the magnetic field H_x for transmission phases of (e) -60° and (f) -30° along the x–y plane in the middle of the unit cell at 10 GHz.....	34
Figure 3.26	Top view of 11 unit cells with topologies 1, 2, or 3.....	35
Figure 3.27	Required phase distributions calculated from Equation (5) for the focusing lens with (a) 100 mm and (b) 60 mm focal distances. Implemented phase distributions of the focusing lens with (c) 100 mm and (d) 60 mm focal distances	36
Figure 3.28	Simulation setup for the focusing lens with a half-wave dipole antenna as a feeding source in symmetry boundaries	37
Figure 3.29	(a) Top view of the fabricated focusing lenses with 100 mm focal distance. (b) Top view of the fabricated focusing lenses with 60 mm focal distance.....	38
Figure 3.3	Setup for measuring the focusing gain of the focusing lens using a half-wave dipole antenna as the feeding source and a standard horn antenna. Both antennas were connected to a vector network analyzer.....	39
Figure 3.31	Simulated and measured and focusing gain patterns on the x–z plane as a function of theta at 10 GHz from the focusing lenses (a) with $f = 100$ mm and (b) with $f = 60$ mm. Simulated and measured focusing gain according to frequency from (c) $f = 100$ mm and (d) $f = 60$ mm.....	40
Figure 3.32	Fractional bandwidth for 100 mm focusing Lens. (a) 1 dB fractional bandwidth (b) 3 dB fractional bandwidth	41
Figure 3.33	Fractional bandwidth for 60 mm focusing Lens. (a) 1 dB fractional bandwidth (b) 3 dB fractional bandwidth	42
Figure 4.1	(a) Side view of electric and magnetic dipole in tunable unit cell. (b) Top view of unit cell. (c) Reconfigurable components PIN and varactor embedded with electric and magnetic dipole. Bias lines are for providing voltage across diodes. The 20 K Ω resistor and DC blocking Capacitor help to block RF and DC current respectively. (d) Sketch of voltage application across diode.....	47

LIST OF TABLES

Table 1	Geometric parameters, simulated electric surface admittance (Y_{es}), magnetic surface impedance (Z_{ms}), transmission phases, and transmission loss of the 11 metasurface unit cells with topologies 1, 2, or 3.....	30
Table 2	Performance comparison of the proposed focusing lenses with the referenced designs.....	43
Table 3	Geometric parameters, simulated electric surface admittance (Y_{es}), magnetic surface impedance (Z_{ms}), transmission phases, and transmission loss of the tuneable metasurface unit cells.....	48

CHAPTER 1: INTRODUCTION

The objective of this chapter is to illustrate a framework and overview of the research work. The whole chapter is divided into two sections motivation and goal, and the thesis organization.

1.1 Motivation and Goal

When designing transmission-type meta-devices, thickness, layer, and efficiency are important factors to consider at the same time. Traditionally, metallic deflectors and dielectric lens were deployed to reform electromagnetics (EM) waves but the large size and weight make them less attractive for millimeter-wave application. Later on, dipoles or patches are placed on a substrate to form transmit-array or reflect-array with flat structures [1]. It is noted that at least three metallic layers are required to simultaneously achieve high transmission amplitude and whole phase coverage [1]. Researchers have investigated many ways to reduce both the thickness and layers.

In [2], ring-split ring transmit-array unit cells nested in a double layer PCB (printed circuit board) was proposed. This structure can cover the whole phase but possess high thickness ($\lambda/3.8$) and high transmission loss (-3 dB). In this structure, the only electric response was considered which made it difficult to achieve thin thickness, high transmittance, and broad bandwidth.

However, to control transmitted field effectively, magnetic responses are also needed to consider, which leads to the development of Huygens' metasurface (HMS). Following the Huygens' Principle, many attempts have been taken to improve transmission performance of the unit cell and to cover the whole phases and at the same time achieve low thickness of PCB structure. In [56], a two-layer and high-efficiency transmissive Huygens' metasurface has been investigated but air space between piled layers made it difficult to manufacture on PCB for practical usability. The other two-layer structures on PCB suffered from high transmission loss (>1 dB) [84-85]. Alternatively, three-layer structures increased transmission efficiency but incurred interference requiring large-scale structural tuning [79-80].

Our goal is to design highly efficient unit cell on a two-layer PCB. We propose three topological structures to cover whole phase with average transmission loss less than 1 dB. The unit structures are comprised of electric and magnetic dipoles with vias. The thickness of the unit cell is $\lambda/18.8$, which implies that both layer and thickness are reduced significantly. These unit cells are used to construct two lenses of 100 mm and 60 mm focal lengths, which can increase the focusing gain of a dipole antenna up to 13 dB. In this proposed design, we not only reduced thickness and layer but also make it easy to implement on PCB. In addition, we cover the whole phase with low average transmission loss and, at the same time, achieve high fractional bandwidth. The 1 dB and 3 dB fractional bandwidth are 13% and 18%, respectively.

Moreover, the unit cell will be used to construct a reconfigurable metasurface by incorporating PIN and varactor diodes. Our goal is to build a single unit cell structure to cover 0° , 90° , 180° , and -90° phases with good transmission performance.

1.2 Thesis Organization

Chapter 2 illustrates the early-stage research on metamaterial and metasurface. More focus is given on transition from 3D structure to 2D structure and continued to metasurface which termed as a zero-thickness sheet. Then, metasurfaces are viewed in terms of application in the field of optics and microwaves. Through this development, Huygens' metasurface emerged and offered efficient wave manipulation characteristics. In this chapter Huygens' metasurfaces are also described from theoretical perspective. This theory describes Generalized Sheet Transition Condition (GSTC). As a result, GSTC is discussed in detail and some literatures are reviewed

which used GSTC.

In chapter 3, the design of focusing lenses by using highly efficient Huygens' metasurface unit cells has been discussed. First, from the literature, two-layer and three-layer structures are considered and debated in terms of their transmission loss and PCB design difficulty. Then, the contribution of this work has been presented. Second, Huygens' metasurface unit cell design method and the detail of three topological structures are described. The difference of these topological structures is shown in terms of their geometrical structure, resonance, surface electric admittance, surface magnetic impedance along the electric and magnetic fields. Third, a detail of lens design procedure based on the distance to phase relationship has been presented. In addition, a simulation setup in high-frequency structure simulator (HFSS) has also been described. Finally, two lenses of 10 mm and 60 mm focal lengths were fabricated and measured. The measurement setup, discussion on the result such as focusing gain and fractional bandwidth have been depicted. Moreover, the superiority of this work has been placed through a comparison with the state of the art of relevant works.

In chapter 4, the passive structure discussed in chapter 4 has been made active/reconfigurable. In this chapter, some recent development in reconfigurable metasurface and some problem in those structures have been discussed. Then, the design method of unit cell and some simulation results have been presented.

Finally, in chapter 6, the overall outcome of the study is summarized as well as few suggestions and future works are also analyzed of this research.

CHAPTER 2: METAMATERIAL AND METASURFACE FUNDAMENTALS AND APPLICATIONS

Metamaterials are artificially constructed and manufactured structural units to achieve desirable properties and functions. Individually built unit cells are distributed in a three-dimensional or two-dimensional lattice to create metamaterials and metasurfaces, respectively.

This chapter illustrates the general background of metamaterial and metasurface and their applications. This chapter also describes Huygens' metasurface from theoretical perspective, reviews different transmitarray structures, and includes the application of Generalized Sheet Transition Condition (GTSC) on metasurface structure. The entire chapter is divided into several sections that contain literature review for background, theory, and Structure design.

2.1 The Metamaterial

Here starts with the idea and history of “metamaterials”: artificial materials that show electromagnetic phenomena that are not found in nature or are not readily available. R. Walser is credited with discovering the concept of composite materials at a DARPA workshop in 1999, where the prefix "meta" was chosen to express that these composites have properties that go beyond those of natural materials. [3-4].

The first explanation of negative refraction sparked a whirlwind of action, as expected. The area was fundamentally multidisciplinary, incorporating topics ranging from physics and materials science to microwave engineering and optics, as well as plasmonics and nanotechnology. Consequently, it triggered immediate and long-term interest from several groups, each encouraged by the potentially unlimited possibilities of finding a new property or application. The persistent efforts of Pendry, notably the discovery that a perfectly constructed negative-index flat lens could theoretically give infinite resolution, breaking the classical diffraction limit, fueled this frenetic speed [5], and his prediction that metamaterials could be used to manipulate optical area in such a way that objects are made invisible [6-7]. These phenomena are demonstrated in experiments [8-11]. Currently, several metamaterial implementations have been evolved in the area of SRR based complementary metamaterial [12] along with magneto dielectric, plasmonic and all-dielectric metamaterials [13-14].

2.2 The Metasurface and Applications

Despite their fascinating wave-manipulation properties, 3-D metamaterials posed a number of issues, including fabrication complexity and high insertion losses. Then 2-D assembly of

engineered particles was investigated to achieve similar interesting properties and applications, now commonly referred to as "metasurfaces". Among many works on metasurface, one early analysis termed artificial rigid surface as “metasurface” [15]. Later impedance surfaces for planar optical metasurfaces were investigated [16-17]. However, in “2003” the term “metasurface” was first used in a published work [18]. The interest grew in the field of metasurface after a groundbreaking work on gradient metasurface, which can manipulate the amplitude and phase of the incident wave [19]. Then, as a fast development, the idea of phased, reflect, transmit arrays and diffraction gratings have been revealed [20-23]. However, it is undeniable that these recent efforts have sparked fascinating technological advances of scientific and commercial importance, as well as increased awareness and interest in metamaterials and metasurfaces.

2.2.1 Application of Metasurface

The spatial variation of elements on a metasurface causes the currents on the surface to lead (or lag) depending on the individual resonant element. This phenomenon helps us to tailor wavefronts as they move through a metasurface, which opens up a wide range of applications. Efficient local control of the form, nature, arrangements, and organization of the components will allow for arbitrary amplitude, phase, and/or polarization manipulation.

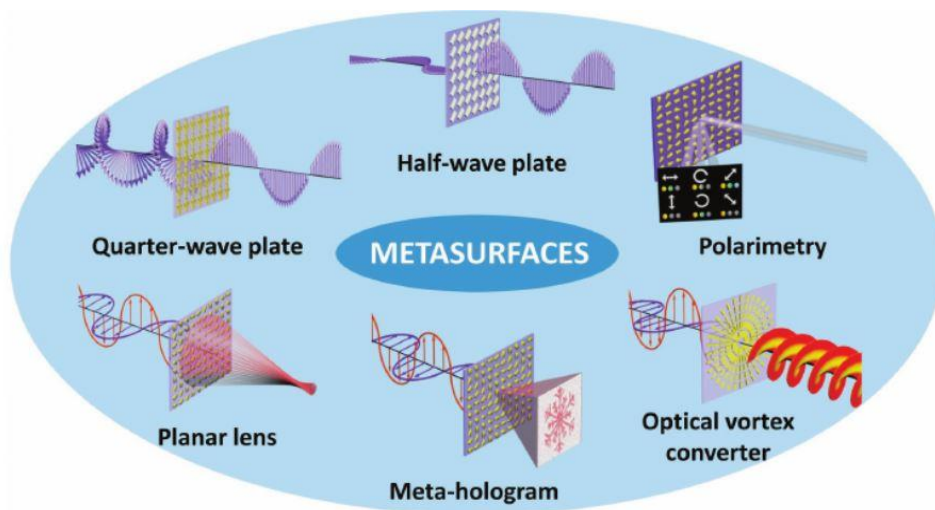


Figure 2.1 Examples of metasurface applications [24].

Metasurfaces are used to manipulate the optical field due to their exceptional light manipulation

abilities. They can eventually lead to the replacement of bulky traditional optical components with compact flat optics. The metasurface has been extensively investigated to realize the traditional functionalities of classic components such as waveplates [25-26], lenses [27-28], beam deflectors [29-30], holograms [31-32], polarimeters [33-34] and optical vortex converters [35], as depicted in Figure 2.1. Some more applications in optical filtering, light absorption, leaky-wave antennas, and nonlinear devices are also investigated [24].

2.3 The Huygens' Metasurface

The amazing ability of metasurface to manipulate light can be realized from the Huygens-Fresnel theory. The classic wave theory of light is analyzed based on the principle introduced by Christian Huygens in 1690 [36]. It explains that any point in space that receives an electromagnetic wave becomes a fictitious source of a new spherical wave moving in the forward direction, illustrating how light spreads gradually. The point sources depicted in Figure 2.2 (a) are known as Huygens sources, and they have long been a purely mathematical concept used to describe various properties in classical wave mechanics, such as refraction (Figure 2.2 b), diffraction, and interference. The theory that underpins the most well-known classes of metasurfaces, those dedicated to wavefront engineering, can be qualitatively explained using this picture. When illuminated, each element on a metasurface can be viewed as a new source that scatters light, creating a secondary source of wavelets, similar to the Huygens theory. In both propagation and reflection, the new wavefronts can be thought of as the sum of all secondary waves. One may construct an artificial interface that forms optical wavefronts into arbitrary shapes by adding spatial variations in the phase retardation of the optical scatterers forming the metasurface. As a result, metasurfaces like these can be thought of as an engineered variant of Huygens' theory.

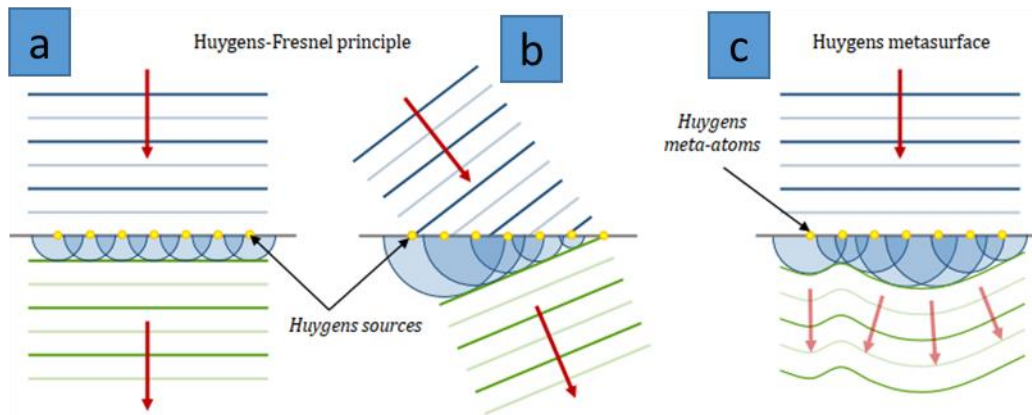


Figure 2.2 (a) - The Huygens-Fresnel theory is shown in this diagram, which depicts the incremental movement of a plane wave through secondary wave excitation. (b) - The Huygens-Fresnel principle is used to explain the event of refraction. (c) – Concept of Huygens' metasurfaces is depicted [37].

According to Huygens' theory, each point on a wavefront acts as a secondary source of outgoing waves [38]. Love developed a more robust version of Huygens' theory in 1901, which described secondary sources in terms of fictitious electric and magnetic currents [39]. Love's Equivalence Principle was later expanded by Schelkunoff to allow for arbitrary field distributions on either side of a surface [40]. The Surface Equivalence Principle, as formulated by Schelkunoff, is widely used in the study of aperture antennas, diffraction problems, and computational electromagnetics formulations [41].

2.4 Theoretical Background of Huygens' Metasurface

The phenomenon explained in section 2.3 can be examined from Maxwell's equations. The differential form can be expressed as:

$$\Delta \times \mathbf{E} = -\mathbf{M}_i - \frac{d\mathbf{B}}{dt} \quad (1)$$

$$\Delta \times H = J_i + J_C + \frac{dD}{dt} \quad (2)$$

$$\Delta \cdot D = \rho_e \quad (3)$$

$$\Delta \cdot B = \rho_m \quad (4)$$

Where E is the electric field intensity, H is the magnetic field intensity, D is the electric flux density, and B is the magnetic flux density. J and M are the electric and magnetic volume current densities, and the subscript i indicates an impressed source, while c indicates a conduction current. In the equations ρ_e and ρ_m are electric and magnetic volume charge densities. J_C is expressed as:

$$J_C = \sigma E \quad (5)$$

Where σ is the conductivity. Electromagnetic boundary condition can be developed from equation (1) to (4) as below:

$$\hat{n} \times (E_2 - E_1) = -M_S \quad (6)$$

$$\hat{n} \times (H_2 - H_1) = J_S \quad (7)$$

$$\hat{n} \cdot (D_2 - D_1) = \rho_{es} \quad (8)$$

$$\hat{n} \cdot (B_2 - B_1) = \rho_{ms} \quad (9)$$

Here \hat{n} is the unit normal to the boundary. J_S and M_S are electric and magnetic surface current densities whereas ρ_{es} and ρ_{ms} are the electric and magnetic surface charge densities. Only a perfect conductor has a non-zero surface current and charge density. Consider a plane wave hitting a dielectric boundary at an oblique angle (see Figure 2.3). In the figure K_{inc} , K_{refr} and K_{refl} are incident, refracted, and reflected wave vectors. Moreover, ϵ and μ are respectively the permittivity and permeability of the mediums.

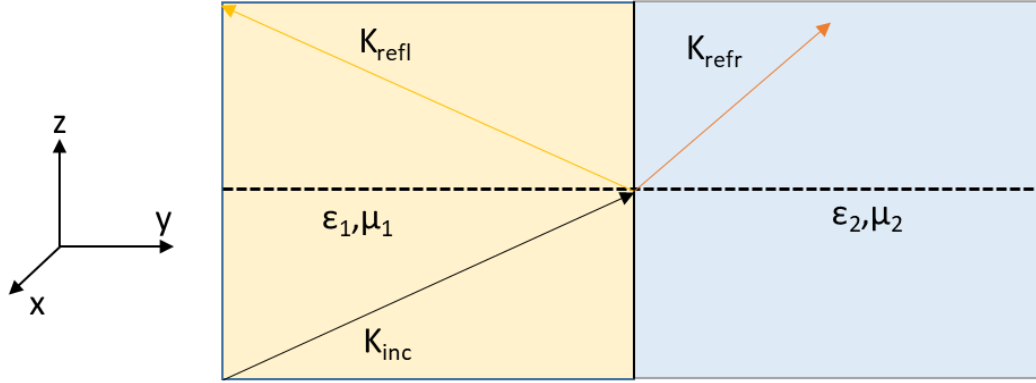


Figure 2.3 Oblique incident of a plane wave at the boundary of two bulk mediums.

Considering equations (6) to (7), the Fresnel coefficients for transmission and reflections can be extracted both for transverse electric (TE) and transverse magnetic (TM) modes [42]. The analysis outcome is as below:

$$\Gamma_{\text{TE}} = \frac{\eta_2 \sec \theta_t - \eta_1 \sec \theta_i}{\eta_2 \sec \theta_t + \eta_1 \sec \theta_i} \quad (10)$$

$$\Gamma_{\text{TM}} = \frac{\eta_2 \cos \theta_t - \eta_1 \sec \theta_i}{\eta_2 \cos \theta_t + \eta_1 \sec \theta_i} \quad (11)$$

$$\mathbf{T}_{\text{TE}} = 1 + \Gamma_{\text{TE}} \quad (12)$$

$$\mathbf{T}_{\text{TM}} = (1 + \Gamma_{\text{TM}}) \frac{\cos \theta_i}{\cos \theta_t} \quad (13)$$

In the above equations η is the intrinsic impedance of the medium. θ_i, θ_t are the incident and transmitted angle whereas Γ and T are the reflection and transmission coefficients, respectively.

Equations (10) to (13) depend on the parameter η . Thus, By engineering ϵ and μ , it is possible to introduce field discontinuities in a volumetric metamaterial to refract a plane wave in any arbitrary fashion as desired. This can be viewed from (8) to (9) which also demonstrates a relationship between B, H , and D, E as well. Now we will look at the case of the Huygens' metasurface, sketched in Figure 2.4.

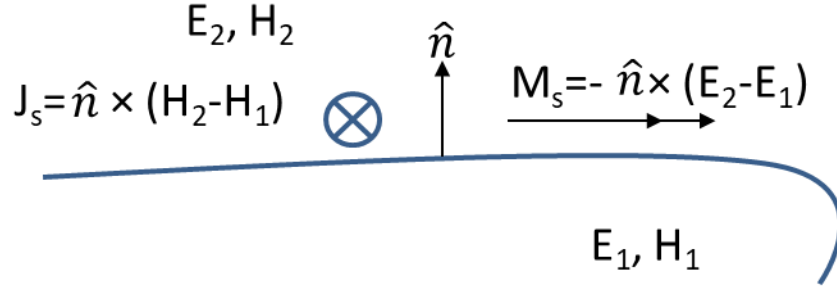


Figure 2.4 A Huygens metasurface with surface current (J_s , M_s) orthogonal at the interface. This current produce transmitted (E_2 , H_2) and reflected field from incident field. E_1 , H_1 are the combination of incident and reflected fields. \hat{n} is normal to the surface [43].

If the medium is not bulk then we can address field discontinuity instead of constitutive parameter, which can be used to change the direction of the plane wave. We can add field discontinuities to adjust the direction of E and H if we can engineer either surface current or charge densities. Surface current densities and surface charge densities produce discontinuous tangential and normal fields, respectively. Only the surface current densities are considered here, and the surface charge densities are assumed to be zero. This is basically Schelkunoff's surface equivalence principle, which is a development of Huygens 'Principle and an expansion of Love's equivalence principle.

Surface currents are interpreted as quantities that can be engineered to achieve the desired effect in this case. As a result, we can see this as an issue of engineering Huygens' sources along a boundary [43]. This analysis can be generalized to arbitrary field distributions around the interface by noting that the fields in (6) to (9) are not limited to plane waves. This issue can also be seen through the framework of surface impedances. The surface current densities are viewed as coming from physical polarization currents produced by an array of polarizable objects to obtain these values. These objects are described as electric and magnetic surface polarizabilities $\overline{\alpha_{es}}$ and $\overline{\alpha_{ms}}$, respectively, which introduce mutual coupling [44]. These polarizabilities are associated with surface current [45] through:

$$J_s = j\omega\overline{\alpha_{es}} E_{t,av}|_s, \quad (14)$$

$$\mathbf{M}_s = j\omega\overline{\overline{\alpha_{mS}}} \mathbf{H}_{t,av}|_s, \quad (15)$$

$\mathbf{E}_{t,av}|_s$ and $\mathbf{H}_{t,av}|_s$ are the average tangential electric and magnetic fields at the boundary. The respective electric and magnetic surface impedances $\overline{\overline{Z_e}}$ and $\overline{\overline{Z_m}}$ are then described.

$$\overline{\overline{Z_e}} = (j\omega\overline{\overline{\alpha_{eS}}})^{-1} = \mathbf{E}_{t,av}|_s / \mathbf{J}_s \quad (16)$$

$$\overline{\overline{Z_m}} = j\omega\overline{\overline{\alpha_{mS}}} = \mathbf{M}_s / \mathbf{H}_{t,av}|_s, \quad (17)$$

Note that Z_e and Z_m are dyadics, corresponding to the anisotropies needed to regulate the input and output fields' polarizations. Combining (6) to (9) with (16) to (17), we can achieve below relationships:

$$\hat{\mathbf{n}} \times \frac{\mathbf{E}_2 + \mathbf{E}_1}{2} = \mathbf{Z}_e \hat{\mathbf{n}} \times (\mathbf{H}_2 - \mathbf{H}_1) \quad (18)$$

$$\hat{\mathbf{n}} \times \frac{\mathbf{H}_2 + \mathbf{H}_1}{2} = -1(1/\mathbf{Z}_m) \hat{\mathbf{n}} \times (\mathbf{E}_2 - \mathbf{E}_1) \quad (19)$$

This implies that the impedances Z_e and Z_m introduce field discontinuities across an interface, resulting in arbitrary field distributions. This is similar to applying equivalent principle for surface current.

2.5 Generalized Sheet Transition Condition (GSTC)

The description in equations (18) and (19) is not considered from the standpoint of polarizability and is named "Generalized Sheet Transition Conditions" (GSTCs) [46]. For simplification full GSTCs consider normal components of the fields. However, an impedance boundary condition and its magnetic dual can be used to model the interaction of subatomic EM fields with a metasurface in a homogeneous medium [47].

The impedance boundary condition is written as

$$\hat{\mathbf{n}} \times (\mathbf{E}_2 - \mathbf{E}_1) = 0 \quad (20)$$

$$\hat{\mathbf{n}} \times (\mathbf{H}_2 - \mathbf{H}_1) = \mathbf{J}_s \quad (21)$$

$$\hat{\mathbf{n}} \times \mathbf{E}_1 = Z_e \mathbf{J}_s \quad (22)$$

Considering magnetic dual, the admittance boundary condition is

$$\hat{\mathbf{n}} \times (\mathbf{E}_2 - \mathbf{E}_1) = -\mathbf{M}_s \quad (23)$$

$$\hat{\mathbf{n}} \times (\mathbf{H}_2 - \mathbf{H}_1) = 0 \quad (24)$$

$$\hat{\mathbf{n}} \times \mathbf{H}_1 = (1/Z_m) \mathbf{M}_s \quad (25)$$

Figure 2.4 can be used to depict (20) to (25). These boundary conditions can be combined to achieve a more compact definition in (18) and (19), as long as the impedances and admittances are collocated and do not couple. A lattice circuit model can be used to relate these impedances to the canonical two-port network parameters [48]. The unit cells are physically designed based on impedance profile by applying transmission line theory, infinite array analysis, and locally periodic approximation [49-50].

We may view electric and magnetic sheet current densities, and thus Z_e and Z_m , as arrays of electric and magnetic dipoles, based on [51]. Infinite magnetic dipoles are the same as infinitesimal electric loops. Surface impedances along the same boundary can thus be engineered using sub-wavelength arrays of collocated electric dipoles and loops, following the equivalence principle. These electric dipoles and loops are implemented as reactive sheets in this work. Pairs of orthogonal collocated electric and magnetic dipoles that correspond to orthogonal electric and magnetic currents, are Huygens' sources. As a result, these metasurfaces are known as "Huygens' Metasurfaces."

2.6 Literature Review on GSTC

In a homogeneous medium, the GSTCs model the interaction of macroscopic EM fields with a metasurface [46]. The GSTCs were not the first, but they are more general than previous attempts, and they provide a review of the literature. This can be linked to the surface currents of the equivalence principle, which were originally defined in terms of macroscopic surface

polarizabilities and later in terms of susceptibilities. These surface currents can be connected to impedances as described in section 2.5. However, in this section, the GSTCs will be only applied to the polarizability and susceptibility formulations, not the impedance formulation. The derivation is detailed in [46], as well as aptly summarized in [52].

In [53], the GSTCs were used to investigate the reflection and transmission of plane waves using a metasurface. In this case, the investigation expands by considering the transmitted and reflected angles are the same as the incident angle. At both TE and TM polarizations, total transmission and reflection are calculated for plane waves of the arbitrary angle of incidence. Negative electric or magnetic susceptibilities can be needed in these circumstances. The Huygens' metasurface, on the other hand, is capable of perfect reflection and transmission for plane waves of arbitrary incidence, reflected, or transmitted angles. This implies that they don't have to be the same. In addition, the metasurface is made up of homogeneous unit cells. The Huygens metasurface, on the other hand, is generally inhomogeneous, allowing for broader applications. In [30], the phenomenon of absolute reflectance and transmission occurring in a metasurface for arbitrary angles of incidence is investigated. However, absolute reflection and transmission with arbitrary incident, reflected, and transmitted angles are still unaddressed.

The GSTCs are further generalized to apply on a material interface [52]. The GSTCs are used to extract parameters from a metamaterial when accounting for boundary effects [54]. In addition, the relationship between a metasurface's surface susceptibilities and its definition in terms of bulk effective medium parameters are investigated in [55]. Here, they vary the thickness of the metasurface. A metasurface is better described as an infinitely thin surface than as a thin layer of bulk media. In this case, the GSTCs' susceptance (or, in our case, impedance) definition is specific to the problem.

CHAPTER 3: FOCUSING LENS WITH HIGH EFFICIENT HUYGENS'

METASURFACE UNIT CELLS

3.1 Literature Review on Huygens metasurface

Metasurface is a two-dimensional structure with subwavelength particles or unit cells for manipulating propagation direction [56–60], polarization [61–66], and orbital angular momentum (OAM) [67–70] of electromagnetic (EM) waves. The ground-breaking feature from the metasurface was introduced from extensive review papers [71–75], and metasurface-based lenses [76–78], antennas [79–82], and holographic imaging [83, 84] have been actively studied. After the advent of a popular metasurface design using the generalized Snell's law [56], which deals with a phase gradient (scalar) on the surface, Huygens' principle was utilized to improve the efficiency of wave-refracting metasurfaces by introducing surface electric and magnetic currents (vector quantities) [57]. Using Huygens' Principle, a metasurface was modeled as a two-dimensional boundary and the required electric and magnetic surface impedances to control the propagation direction of a transmitted wave was achieved [57].

3.1.1 Generalized Laws of Reflection and Transmission

The phase discontinuity at the boundary of two media forces us to reconsider Fermat's Principle. Suppose a plane wave impinges on the surface with angle θ_i . In Figure 3.11 two paths are shown which if infinitesimally close to the actual light way then zero phase difference will be shown

$$[k_o n_i \sin(\theta_i)dx + (\phi + d\phi)] - [k_o n_t \sin(\theta_t)dx + \phi] = 0 \quad (26)$$

In the equation, θ_t refraction angle and phase discontinuity at the interface for two paths are ϕ and $\phi + d\phi$. The distance between two intersection points is dx whereas n_i and n_t are medium refractive indices and $k_o = 2\pi/\lambda$, where λ free-space wavelength. Equation (26) turns to generalize Snell's law for transmission if the phase gradient along the surface is constant.

$$n_t \sin(\theta_t) - n_i \sin(\theta_i) = \lambda/2\pi \times d\phi/dx \quad (27)$$

Equation (27) shows that refracted wave can have arbitrary direction.

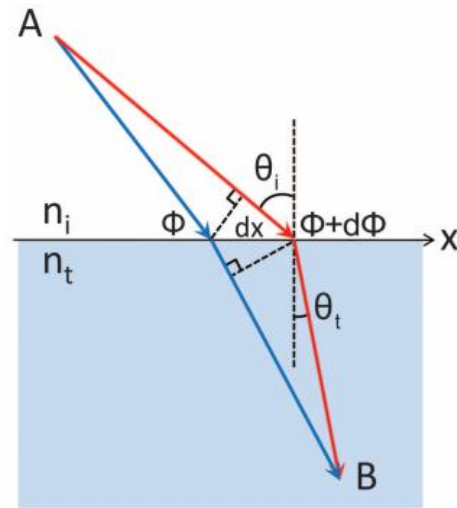


Figure 3.11 Sketch of generalize Snell's law of refraction. The phase shifts are ϕ and $\phi + d\phi$ where blue and red paths crossed the boundary [56].

3.1.2 Two-Layer Structures on printed circuit board (PCB)

Metasurface design based on Huygens' principle is theoretically sound; however, it is not straightforward to implement electric and magnetic surface impedances that cover a wide transmission phase range with high transmission efficiency in a planar 2D structure, e.g., printed circuit board (PCB). In [57], Pfeiffer et al. designed electric and magnetic dipoles in two-layer PCB strips but had to stack the strips between air space (see Figure 3.12.) to align the vector components of the incident electric and magnetic fields with the corresponding surface impedance vectors.

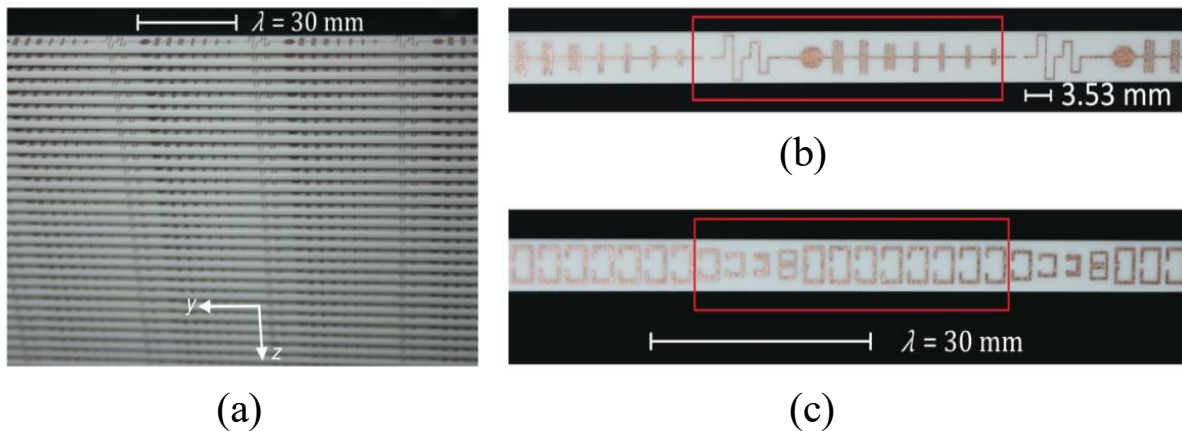


Figure 3.12 (a) Fabricated Huygens Surface. (b) Top view which provides electric polarization current (c) Bottom structure for magnetic polarization current [57].

More fabrication-friendly unit cells with the required surface impedances have been designed and laid out in two-layer PCBs, but the unit cells were not able to maintain low transmission loss (<1 dB) (see Figure. 3.13 and 3.14) for all the required surface impedances, especially high electric and magnetic resonance cases [85–92].

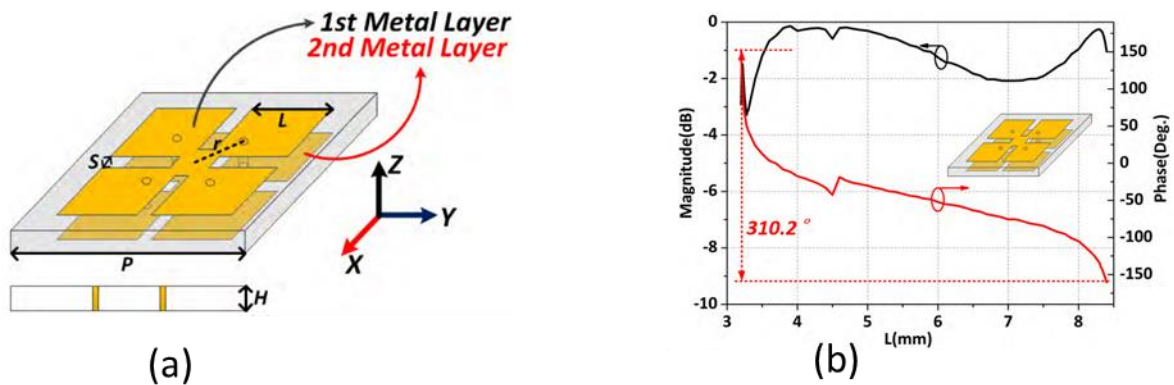


Figure 3.13 (a) Transmit Unit cell of two-layer. (b) S_{21} Parameters of the Unit cell. [89]

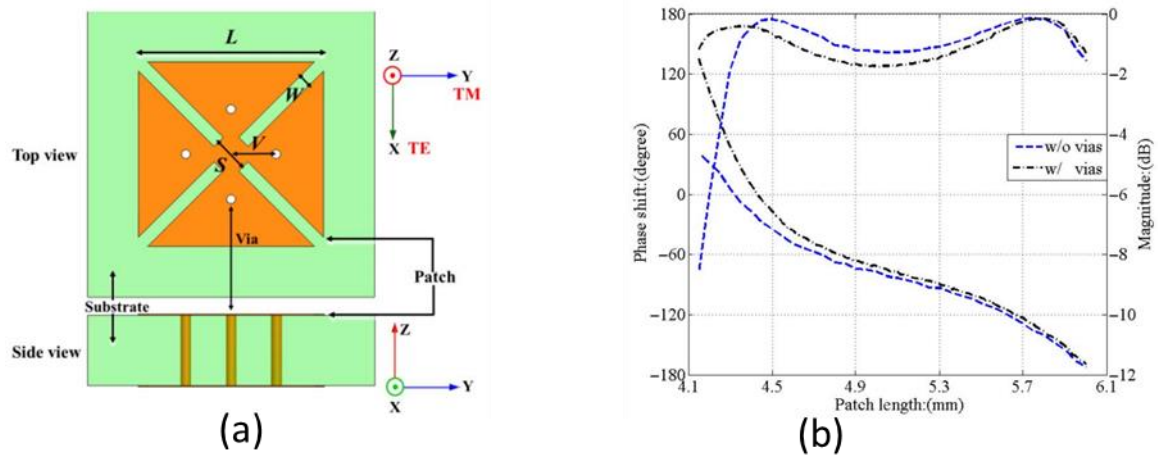


Figure 3.14 (a) Top and side view of two-layer unit cell with via. (b) Transmission performance of unit cell. [90]

3.1.3 Three-Layer Structures

For better efficiency, a three-layer PCB capable of generating a loop current from the first and third layers using two vias was implemented [93–95]. Recently, in the same three-layer PCBs, symmetric and asymmetric unit cells with two magnetic dipoles (dogbone shape) on the top and bottom layer and an electric dipole (capacitor-loaded dipole) in the middle layer have been implemented [78,81,96,97]. This three-layer structure is shown in Figure 3.15. Despite the higher transmission efficiency of these three-layer unit cells, the drawbacks can be increased geometrical parameters that need to be tuned and interference by waves propagating along the multiple layers, which require optimization.

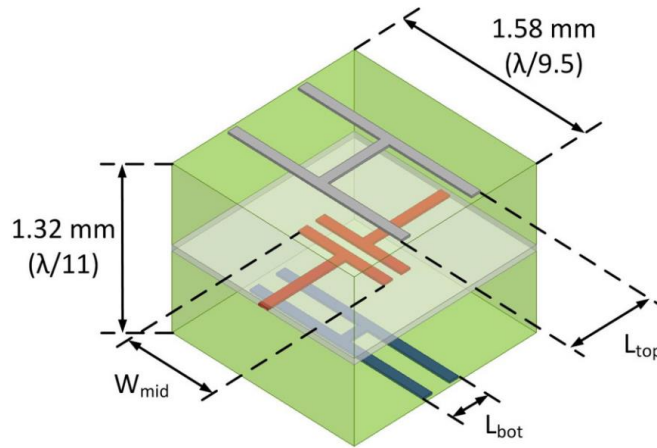


Figure 3.15 Dog bones and loaded dipole structure of three-layer. [97]

3.1.4 This Work

In this paper, we introduce double-layer metasurface unit cells with high transmission efficiency and wide phase coverage at 10 GHz by constructing electric and magnetic dipole structures based on Huygens' Principle. In the unit cells, electric and magnetic dipoles were implemented in 1.6 mm-thick ($\approx\lambda/18.8$) double-layer FR4 PCB and via drills were used to form antisymmetric conducting loops for magnetic dipole resonance by connecting top and bottom metallic traces. Vias were also implemented in the electric dipole structure and the desired capacitance of the unit cell was achieved. Overall, we designed 11 unit cells to cover transmission phases from -150° to 150° and achieved a low average transmission loss of -0.82 dB at 10 GHz. To assess the practical

performance of the unit cells, we designed two compact lenses with near $5\lambda \times 5\lambda$ (152.1×156 mm) size to focus a spherical beam to specific focal points of 100 mm ($f/D = 0.65$) and 60 mm ($f/D = 0.39$). The lenses were designed for such low f/D values to be used for a compact and low profile transmit-array [101, 102]. From the fabricated devices, radiated power from the half-wave dipole located at the focal distances was enhanced by 12.87 and 13.58 dB at 10 GHz for $f/D = 0.65$ and 0.39 cases, respectively, and a wide 1 dB gain bandwidth near 10% was demonstrated.

3.2 Huygens' Metasurface Unit Cell Design

3.2.1 Unit Cell Design Method

The generalized sheet transition condition (GSTC) models a metasurface as electric and magnetic polarizability densities (α_{ES} and α_{MS}) and relates those to the transmission coefficient (T) and reflection coefficients (R) of the metasurface [53]. Then, using Equations (1) and (2), α_{ES} and α_{MS} can be converted to the electric surface admittance (Y_{es}) and magnetic surface impedance (Z_{ms}), which are familiar concepts from Huygens' Principle. Here, we assume isotropic surface electric admittance and magnetic impedance.

$$Y_{es} = j\omega\varepsilon\alpha_{ES} \quad (28)$$

$$Z_{ms} = j\omega\mu\alpha_{MS} \quad (29)$$

By the simple conversion, the normalized values of $Y_{es}\eta_0$ and Z_{ms}/η_0 are given in terms of T and R in Equations (30) and (31). It is important to note that these simple equations can be derived when the propagation directions of the incident and transmitted waves are normal to the boundary [53]. More general equations with the arbitrary incident and transmitted angles were also derived in [100].

$$Y_{es}\eta_0 = 2 \frac{1 - T - R}{1 + T + R} \quad (30)$$

$$Z_{ms}/\eta_0 = 2 \frac{1 - T + R}{1 + T - R} \quad (31)$$

Here, η_0 is the intrinsic impedance of free space. Equations (30) and (31) indicate that a reflectionless ($R = 0$) metasurface requires the same values of $Y_{es}\eta_0$ and Z_{ms}/η_0 . To maintain

almost perfect transmission ($T = 1$) with wide transmission phase variation, only the imaginary part of Y_{es} and Z_{ms} should be utilized. Figure 3.16 shows that the simultaneous change of $\text{Im}\{Y_{es}\eta_0\}$ and $\text{Im}\{Z_{ms}/\eta_0\}$ from -15 to 15 covers transmission phases from -165° to 165° . Here, $Y_{es}\eta_0$ and Z_{ms}/η_0 are purely imaginary numbers.

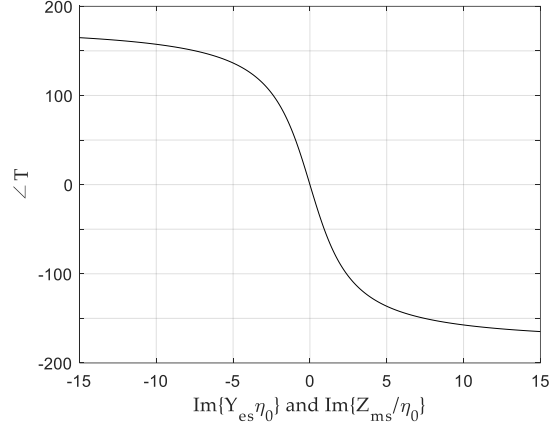


Figure 3.16. Transmission phases versus the imaginary part of the normalized surface electric admittance $\text{Im}\{Y_{es}\eta_0\}$ and the normalized surface magnetic impedance $\text{Im}\{Z_{ms}/\eta_0\}$.

3.2.2 Unit Cell Dimension

First, we determined one period (42.42 mm) of the metasurface units which needs to cover 360° transmission phase range to refract normal incident beam to 45° using $\lambda/\sin 45^\circ$ at 10 GHz. To have enough discretization, we chose 11 unit cells in one period and fixed the width of the unit cell to 3.9 mm. The unit cell thickness was then fixed with 1.6 mm from the given FR4 substrate. Finally, we varied the length of the unit cell using a structure for $+150^\circ$ transmission phase and found the optimum length of 6 mm for the highest transmission at 10 GHz as shown in Figure 3.17.

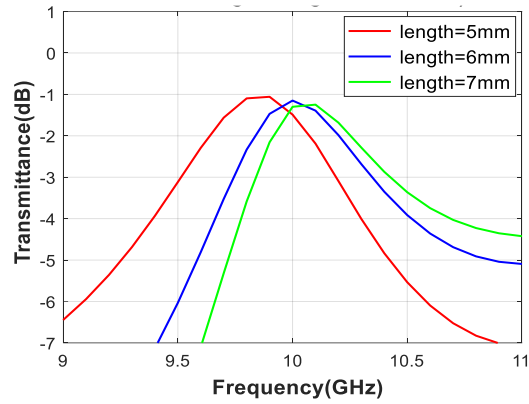


Figure 3.17 Transmittance along the frequency from different unit cell lengths.

3.2.3 Unit Cell Topology Design and Analysis

We designed unit cells to provide desired normalized Y_{es} and Z_{ms} values to cover a wide range of transmission phases ($-150^\circ \sim 150^\circ$) with low transmission loss (< 1 dB) at 10 GHz. Instead of using one topology for all the phases, we designed three optimum unit cell topologies for specific transmission phase ranges. First, we designed a unit cell with a high positive Y_{es} and Z_{ms} to realize the -150° transmission phase with low transmission loss. Generally, electric dipole resonance can be implemented easily with capacitor-like structures and is stronger than magnetic resonance. To increase magnetic resonance strength, which should match the electric resonance strength, we implemented two magnetic dipoles on the sides and one electric dipole at the center using vias, as shown in Figure 3.18.

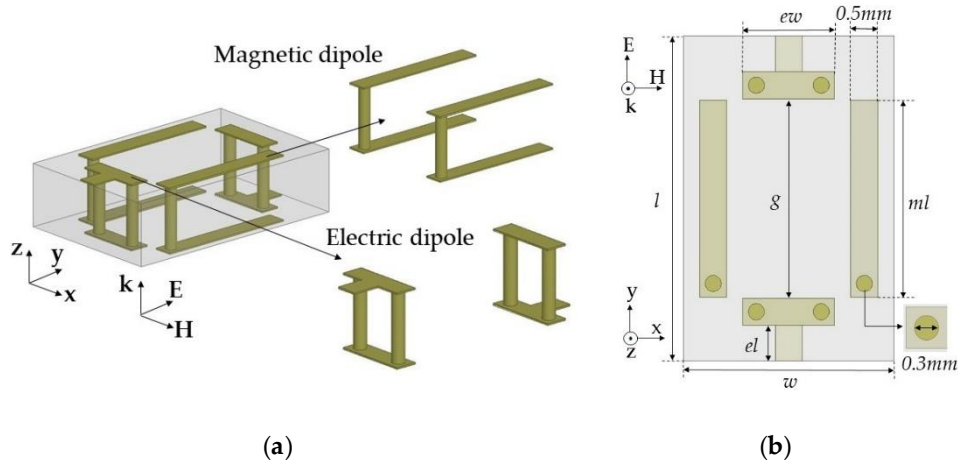


Figure 3.18. Electric and magnetic dipole in topology 1 from the (a) side-side view and (b) top view.

Here, the alignment of both dipoles was based on a y-polarized TEM wave propagating along the z-axis. The unit cells were simulated using Ansys high frequency structure simulator (HFSS) and the excitation and boundary conditions were used with wave ports and perfect electric conductor (PEC)/perfect magnetic conductor (PMC) boundaries, respectively. In the design, we used a 1.6 mm-thick double-layer FR4 substrate with a relative permittivity (ϵ_r) of 4.3 and loss tangent ($\tan \delta$) of 0.008. The unit cell area was fixed to a length (l) of 6 mm and width (w) of 3.9 mm. We used the rectangular-shaped unit cell to support long asymmetric current flow and a close space between the two magnetic dipoles to achieve a high Z_{ms} value and a low discretization error along the x-axis. Geometrical parameters of the unit cell included ml (the length for the magnetic dipole), g (the gap between the capacitively coupled electric dipoles), and ew (the width of the capacitor of the electric dipoles). Last, el indicates the electric dipole length, which is dependent on g . Therefore, we varied ml for the desired Z_{ms} values and g and ew for the Y_{es} tuning. One benefit of this unit cell topology is that electric and magnetic resonance can be controlled independently because both electric and magnetic structures are implemented perpendicularly by the intuition of Huygens' surface electric and magnetic currents. Finally, a unit cell with $ml = 3.64$ mm, $g = 3.68$ mm, and $ew = 1.7$ mm achieved high Y_{es} and Z_{ms} values of 7.55 and 5.87, respectively, with an S_{21} of -0.96 dB and -150° transmission phase. To balance Y_{es} and Z_{ms} , Y_{es} resonance where the peak of Y_{es} occurs

has to be located near 12.4 GHz, which was implemented with lower capacitance by using a wide gap distance ($g = 3.68$ mm) between the two electric dipoles, as shown in Figure 3.19 b. However, the Z_{ms} resonance should be near 10 GHz to achieve a sufficiently high Z_{ms} value to match the Y_{es} value at 10 GHz. Figure 3.19 c shows a high magnetic field excited along the x-axis due to current flows on the magnetic dipoles.

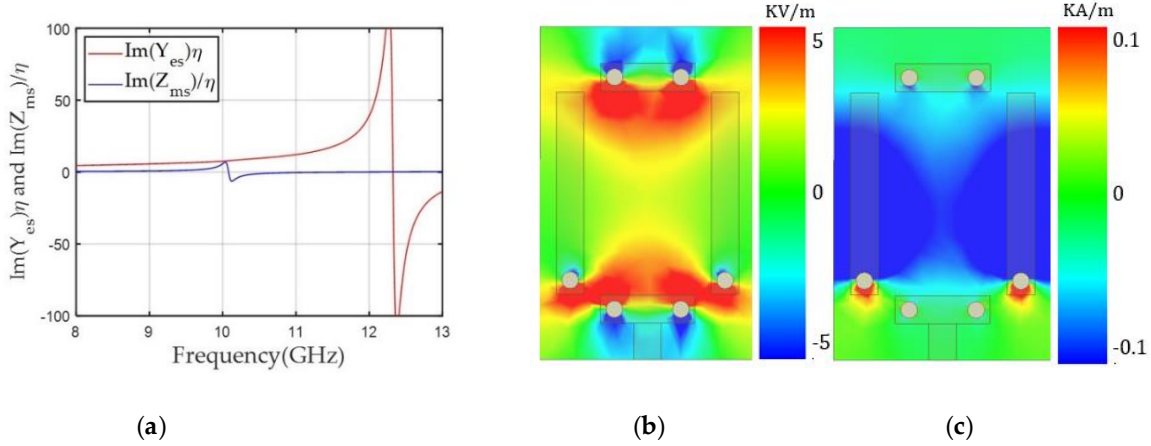


Figure 3.19. (a) Y_{es} and Z_{ms} values of the unit cell according to frequency for a transmission phase of -150° . (b) The y component of the electric field E_y . (c) The x component of the magnetic field H_x along the x–y plane in the middle of the unit cell at 10 GHz.

Next, we reduced the Y_{es} and Z_{ms} resonance frequencies to achieve balanced negative values for both Y_{es} and Z_{ms} at 10 GHz for the $+150^\circ$ transmission phase, as shown in Figure 3.2 a. Based on the unit cell with a transmission phase of -150° , the gap (g) of the electric dipole was lowered up to 1.30 mm and the magnetic dipole length (ml) was decreased to 3.61 mm. This structure moved the Y_{es} and Z_{ms} resonance frequencies to 8.2 and 9.8 GHz, respectively, and achieved balanced Y_{es} (-7.19) and Z_{ms} (-7.15) at 10 GHz, providing -1.1 dB S_{21} with $+150^\circ$ phase. Figure 3.2 b,c shows the unit cell structure for the $+150^\circ$ phase and E_y and H_x on the x–y plane in the middle of the structure. E_y was confined near the gap of the electric dipole’s capacitor structure, which was responsible for the lower resonance frequency of Y_{es} compared to the unit cell for the -150° phase. Figure 3.2 c shows that the strong x components of the magnetic field were

distributed in the middle of the magnetic dipoles, lowering the resonance frequency of Z_{ms} and yielding a negative Z_{ms} value at 10 GHz.

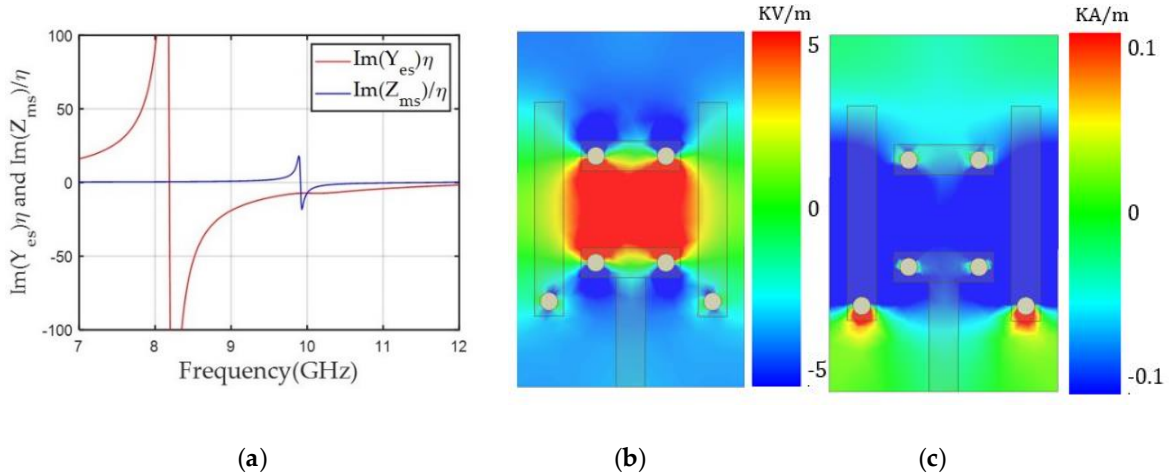


Figure 3.2. (a) Y_{es} and Z_{ms} values of the unit cell along frequency for a transmission phase of $+150^\circ$. (b) The y component of the electric field E_y . (c) The x component of the magnetic field H_x along the x-y plane in the middle of the unit cell at 10 GHz.

We realized the unit cells for the other positive phases from $+120^\circ$ to 0° by lowering negative Y_{es} and Z_{ms} values at 10 GHz. To do that, we lowered the resonance frequency of Y_{es} and Z_{ms} by reducing the gap of the electric dipole (g) and tuning the electric dipole width (ew), and increasing the length of the magnetic dipole (ml), respectively. Figure 3.21 a shows the normalized Y_{es} and Z_{ms} values from the unit cell for $+120^\circ$ with $g = 0.37$ mm, $ew = 1.0$ mm and $ml = 3.70$ mm. The balanced Y_{es} and Z_{ms} values of -3.5 and -3.3 at 10 GHz are shown; this condition provided a low S_{21} of -1.1 dB. As shown in Figure 3.21 b, c, E_y and H_x from the unit cell with $+120^\circ$ had a similar confined E_y field near a smaller gap of the electric dipole and stronger magnetic field due to a longer ml compared to the unit cell for the $+150^\circ$ phase. This phenomenon corresponded to lower Y_{es} and Z_{ms} resonance frequencies in the $+120^\circ$ phase structure. We decreased the Y_{es} and Z_{ms} resonance frequencies by using a more confined E_y and higher H_x , and finally covered phases from $+90^\circ$ to 0° . Detailed geometries and Y_{es} and Z_{ms} values are shown in Table 1.

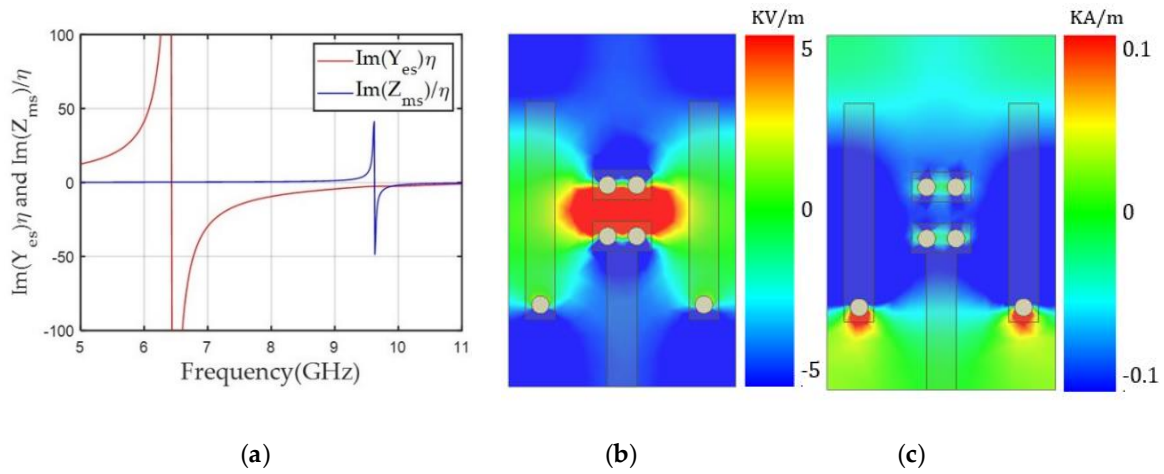


Figure 3.21. (a) Y_{es} and Z_{ms} values of the unit cell according to frequency for a transmission phase of $+120^\circ$. (b) The y component of the electric field E_y . (c) The x component of the magnetic field H_x along the x–y plane in the middle of the unit cell at 10 GHz.

Table 1. Geometric parameters, simulated electric surface admittance (Y_{es}), magnetic surface impedance (Z_{ms}), transmission phases, and transmission loss of the 11 metasurface unit cells with topologies 1, 2, or 3.

Cell	Topology	g (mm)	g1 (mm)	g2 (mm)	m1 (mm)	ew (mm)	Im (Y_{es})	Im (Z_{ms})	Trans. phase ($^\circ$)	Trans. loss (dB)
1	1	0.20			4.60	1.7	0	0	0	-0.4
2	1	0.20			4.15	1.7	-1.1	-0.2	30	-1.1
3	1	0.20			3.72	2.1	-1.5	-0.9	60	-1.0
4	1	0.20			3.76	1.0	-2.4	-1.7	90	-1.0
5	1	0.37			3.70	1.0	-3.5	-3.3	120	-1.1
6	1	1.30			3.61	1.7	-7.19	-7.15	150	-1.1
7	1	3.68			3.64	1.7	7.55	5.87	-150	-0.96
8	1	4.60			3.61	1.7	3.9	2.8	-120	-0.72
9	2				3.47	2.0	2.8	1.4	-90	-0.72
10	3		0.5	0.8	3.6		1.4	0.88	-60	-0.59
11	3		1	0.6	2.8		0.7	0.4	-30	-0.34

For negative transmission phases, we used the unit cell for -150° and achieved -120° by increasing the Y_{es} and Z_{ms} resonance frequencies. For lower effective capacitance and inductance of the unit cell, the gap (g) between the electric dipole was increased from 3.68 to 4.60 mm and the magnetic dipole length (ml) was shortened from 3.64 to 3.61 mm. Finally, lower positive Y_{es} (3.9) and Z_{ms} (2.8) values at 10 GHz were achieved with a low S_{21} of -0.72 dB. Figure 3.22a shows the Y_{es} and Z_{ms} values according to frequency for the unit cells for the -150° and -120° phases. Lower Y_{es} and Z_{ms} values were observed for the -120° case at 10 GHz due to the higher Y_{es} resonance frequency near 14.8 GHz. The lower Z_{ms} value in the -120° case was due to a resonance frequency shift to a higher frequency near 10.2 GHz. Figure 3.22b shows that E_y for the unit cell with the -120° phase was distributed over a larger area than observed for the -150° case (Figure 3.19.a). Figure 6c for H_x also shows lower magnetic fields between two magnetic dipoles. Both trends correspond to higher resonance frequencies for both Y_{es} and Z_{ms} and lower values at 10 GHz for the -120° case.

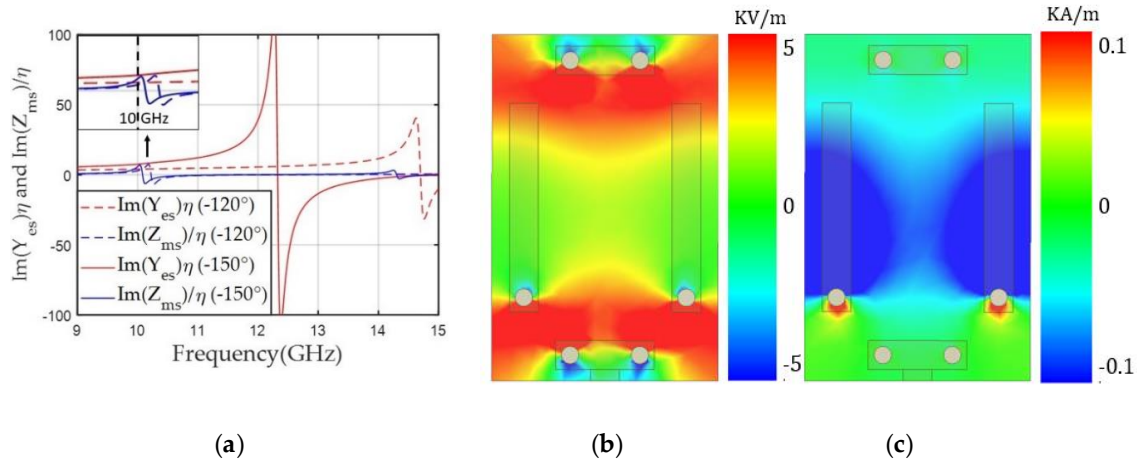


Figure 3.22. (a) Y_{es} and Z_{ms} values of the unit cell according to frequency for transmission phases of -150° and -120° . (b) The y component of the electric field E_y for the transmission phase of -120° . (c) The x component of the magnetic field H_x for -120° along the x-y plane in the middle of the unit cell at 10 GHz.

For the -90° transmission phase, lower positive Y_{es} and Z_{ms} are needed; however, the gap of the electric dipole (g) cannot be further increased due to fabrication limits. Therefore, we used one electric dipole structure to provide a lower Y_{es} at 10 GHz and two magnetic dipoles

were maintained, as shown in Figure 3.23a. The geometrical parameters are shown in Figure 3.23b; an ew of 2 mm and ml of 3.47 mm provided a normalized Y_{es} of 2.8 and Z_{ms} of 1.4, resulting in the achievement of a -90° phase with a low S_{21} of -0.72 dB. Figure 3.23c shows that Y_{es} and Z_{ms} values became lower at 10 GHz due to Z_{ms} and Y_{es} resonance frequencies higher than 10 GHz. Figure 3.23d,e shows that E_y was distributed over a larger area and H_x was weaker in the -90° case than the -120° case.

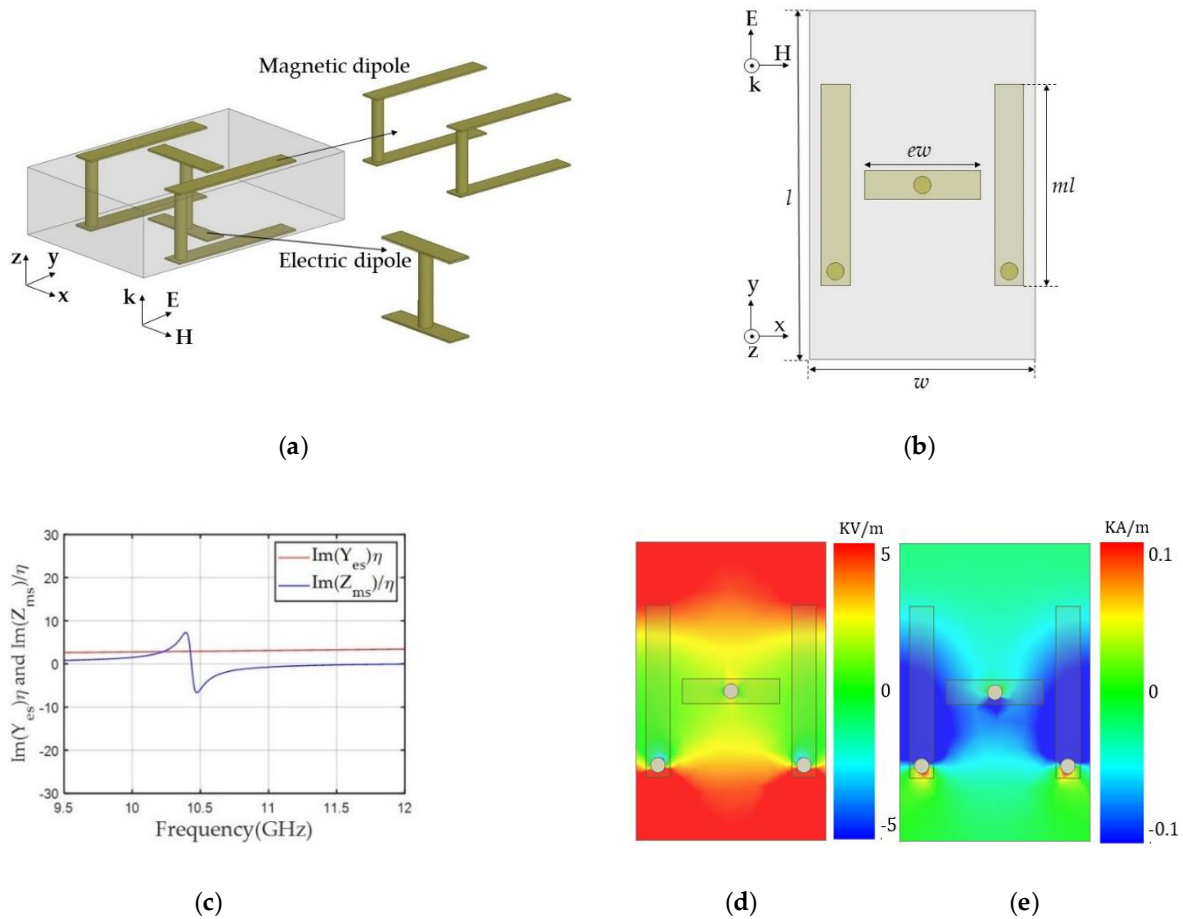


Figure 3.23. Electric and magnetic dipoles in the topology 2 structure from the (a) side-side view and (b) top view. (c) Y_{es} and Z_{ms} values of the unit cell according to frequency for a transmission phase of -90° . (d) The y component of the electric field E_y . (e) The x component of the magnetic field H_x along the x-y plane in the middle of the unit cell at 10 GHz.

To further reduce Y_{es} and Z_{ms} to cover the -60° and -30° transmission phases, we used one magnetic dipole in the center of the unit cell and located the electric dipoles around the boundary of the unit cell on the top and bottom layers, as shown in Figure 3.24a. Figure 3.24b shows the geometrical parameters of topology 3. The length of g_3 was fixed at 0.5 mm and horizontal gaps (g_1 and g_2) between the magnetic and the electric dipole structures, and magnetic dipole length (ml) were mainly tuned to control the near-zero Y_{es} and Z_{ms} accurately such that Y_{es} and Z_{ms} became 0.7 and 0.4 for the -30° case. Here, ml and g_2 determine the vertical length of the electric dipole. Finally, we achieved almost zero transmission loss for the -30° and -60° cases (-0.34 and -0.59 dB, respectively). This topology achieved near-zero Y_{es} values at 10 GHz because maximum Y_{es} resonance frequencies were located under 8 GHz and the zero-crossing Y_{es} frequency was near 10 GHz, as shown in Figure 3.25a,b. Similar to the other negative phase cases, Z_{ms} resonance frequencies were higher than 10 GHz, resulting in near-zero Z_{ms} values at 10 GHz. Figure 3.25c,d shows that E_y was distributed along the entire area of the unit cells for transmission phases of -60° and -30° , in contrast to the other negative phase cases. We attributed the wide distribution of E_y to the near-zero Y_{es} at 10 GHz for both cases. Compared to the -60° case, the -30° case showed a more distributed E_y ; therefore a slightly higher Y_{es} value was achieved in the -60° case. Figure 3.25e,f shows that the -60° case had higher magnetic fields along the x-axis, resulting in a higher Z_{ms} value at 10 GHz.

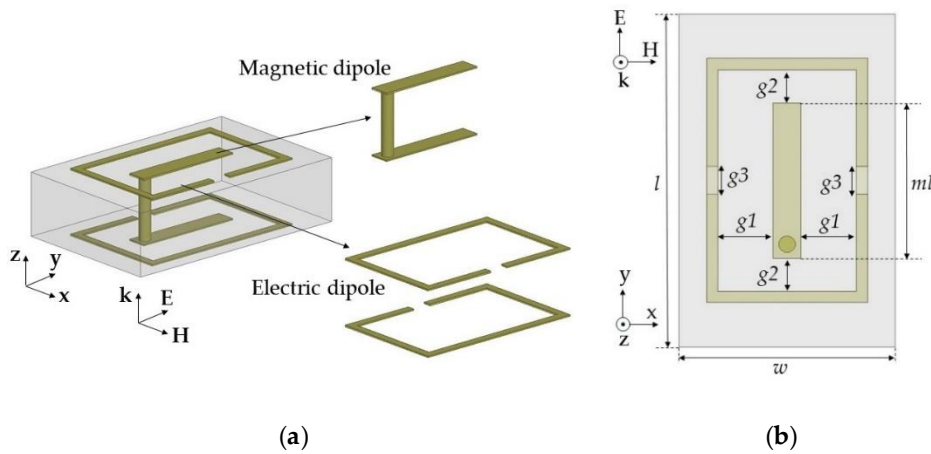


Figure 3.24. Electric and magnetic dipoles in the topology 3 structure from the (a) side–side view and (b) top view.

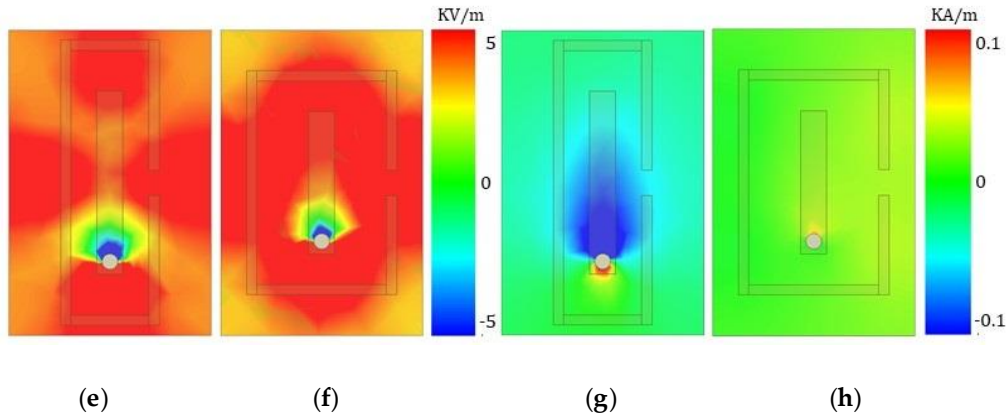
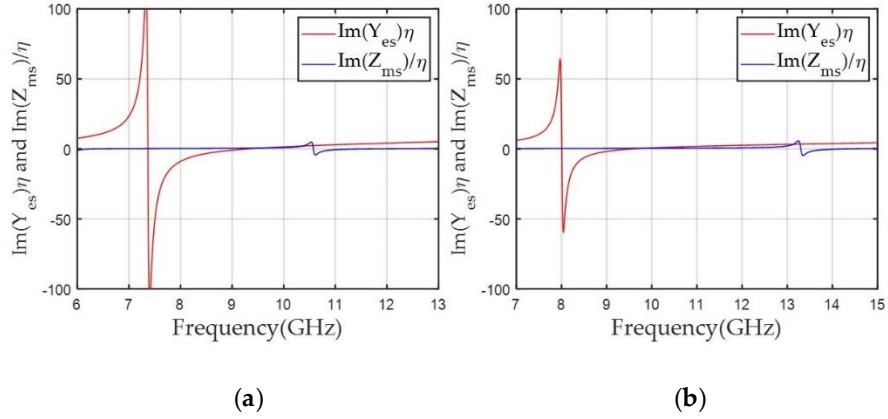


Figure 3.25. Y_{es} and Z_{ms} values of the unit cell according to frequency for transmission phases of (a) -60° and (b) -30° . The y component of the electric field E_y for transmission phases of (c) -60° and (d) -30° . The x component of the magnetic field H_x for transmission phases of (e) -60° and (f) -30° along the x–y plane in the middle of the unit cell at 10 GHz.

Figure 3.26 provides a top view of all the unit cells with topologies 1, 2, or 3. Y_{es} and Z_{ms} values of the corresponding unit cells and their transmission parameters are presented in Table 1. The highest and lowest transmission loss levels were -1.1 and -0.34 dB, respectively, and the average loss was -0.82 dB, which was lower than the average S_{21} of -1.04 dB reported for a similar double-layer PCB-based unit cell operating at 10 GHz [87]. Moreover, previously reported structures had a maximum transmission loss of -2.5 dB, while that of the proposed

unit cells was -1.1 dB. These findings demonstrate that unit cell topologies optimized for specific transmission phases significantly reduce transmission loss of the overall unit cells

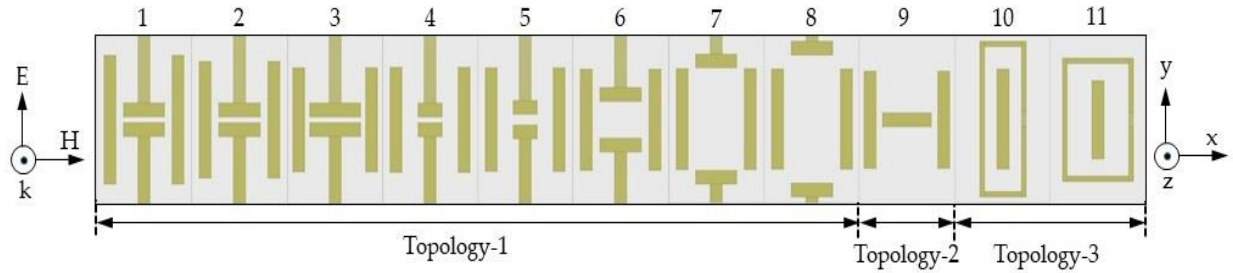


Figure 3.26. Top view of 11 unit cells with topologies 1, 2, or 3.

3.3 Focusing Lens Design

Based on the high transmission efficiency of the 11 unit cells covering the -150° to 150° phases, we designed two focusing lens structures to collimate incident spherical waves radiated from short distances. Because the designed unit cells had subwavelength dimensions of $w = 3.9$ mm ($\lambda / 7.7$) and $l = 6$ mm ($\lambda / 5$), we were able to design a compact-sized ($5\lambda \times 5\lambda$) array with short focal points (f) of 100 and 60 mm. Both 100 and 60 mm focal points means low f/D numbers of 0.65 and 0.39, respectively, that would be needed for a compact focusing lens-integrated system.

3.3.1 Distance to Phase Relationship

The required transmission phases (ϕ_i) to collimate the spherical waves from both focal points were determined from Equation (32), as shown in Figure 3.27 a, b, and the corresponding unit cells were arranged accordingly. The target phases, drawn in Figure 3.27 a, b, were discretized using 30° steps.

$$\phi_i = k_0(R_i - f) + \phi_0 \quad (32)$$

In Equation (32), R_i is the distance between the center of the unit cell element and the focal point and f is the focal distance. We used the wavenumber (k_0) from the 10 GHz frequency and set ϕ_0 to -150° as the default phase at the center of the array where R_i and f are equal. One thing to note is

that due to the unit cells' compact size, steeper phase changes required for short focal distances could be realized with a low discretization error. Finally, we arranged different numbers of rectangular-shaped (3.9×6 mm) unit cells along the x-axis (39 cells) and y-axis (26 cells) to realize a near $5\lambda \times 5\lambda$ -sized (152.1×156 mm) focusing lens. Figure 3.27 c, d shows the implemented phase distribution of both focusing lenses. Because the calculated phases near the center of the focusing lenses were located in the middle of the 30° phase gap of the unit cells, a slight phase difference between Figure 3.27 a, b and Figure 3.27 c, d near the center area was allowed in the design process.

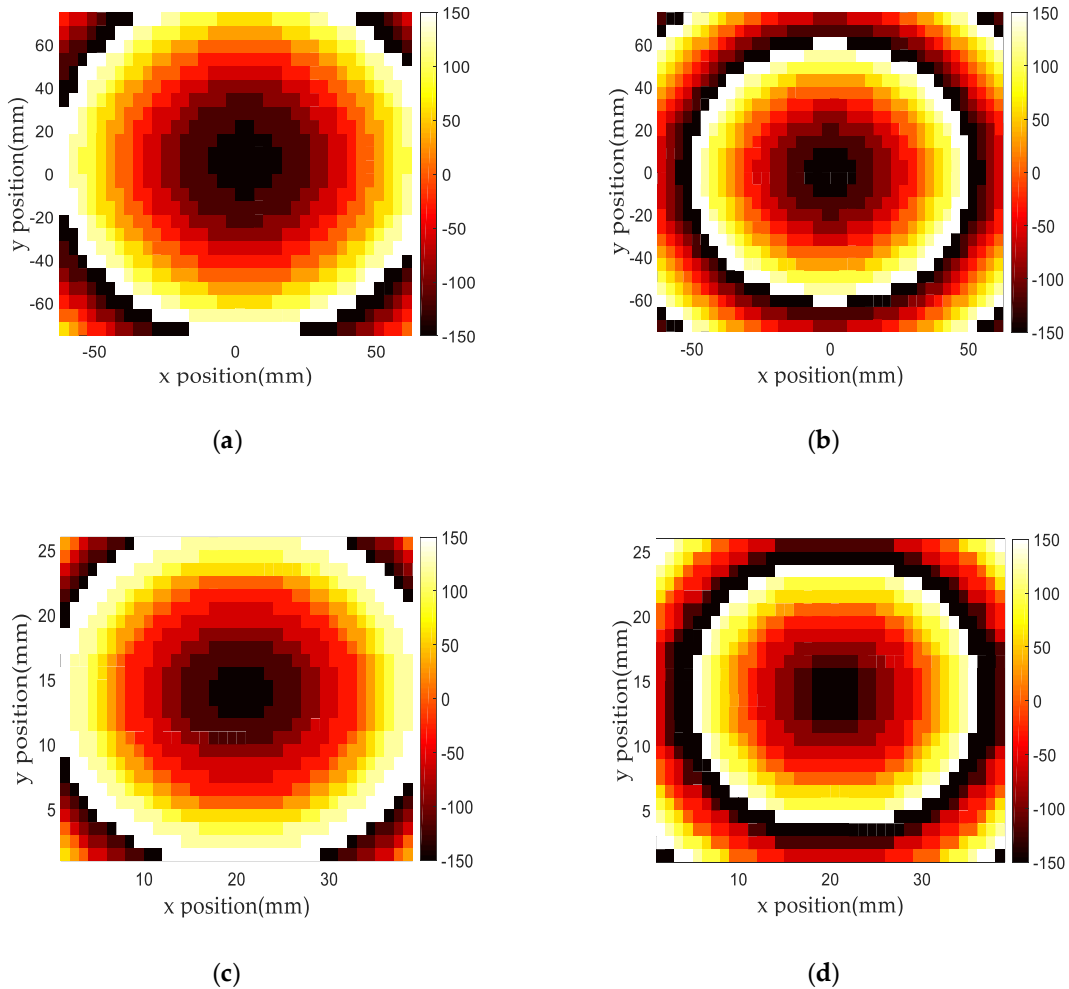


Figure 3.27. Required phase distributions calculated from Equation (5) for the focusing lens with (a) 100 mm and (b) 60 mm focal distances. Implemented phase distributions of the focusing lens with (c) 100 mm and (d) 60 mm focal distances.

3.3.2 Simulation Setup

In simulations, both focusing lenses with 3D unit cell structures were implemented in HFSS and the focusing gain was calculated. For the simulation load reduction, a quarter of the focusing lens in the first quadrant was used with symmetric boundaries in the simulation tool (see Figure 3.28). A spherical wave as the incident wave was implemented by a half-wave dipole antenna operating at 10 GHz at a focal distance from the focusing lens. The focusing gain, defined as the gain from the focusing lens–combined dipole antenna minus the gain of the dipole antenna at the boresight [104–107] was calculated as 13.47 and 14.09 dB at 10 GHz for $f = 100$ and 60 mm, respectively. Gain patterns from the simulations were compared with those obtained experimentally (see below).

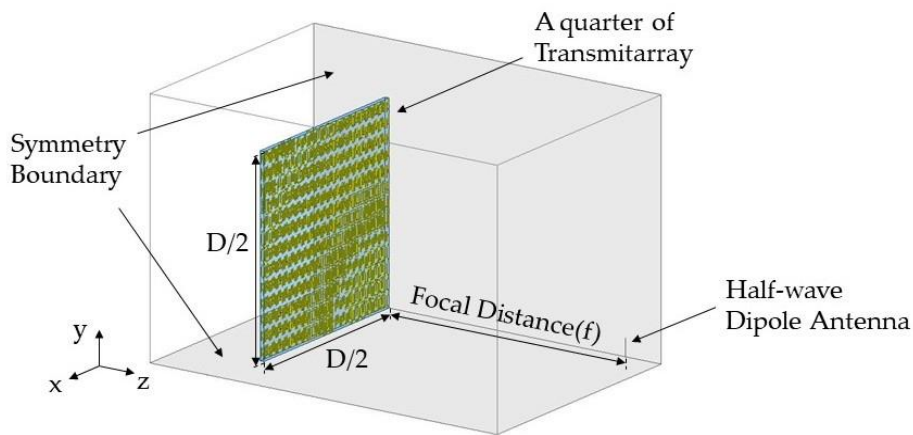


Figure 3.28. Simulation setup for the focusing lens with a half-wave dipole antenna as a feeding source in symmetry boundaries.

3.4 Fabrication and Measurement

For experimental verification, both focusing lenses with the same PCB size (156×160 mm) for $f = 100$ and 60 mm were fabricated, as shown in Figure 3.29(a) and (b). Extra spaces on the boundary were added for stable patterns and via fabrication based on the designed size of 152.1×156 mm.

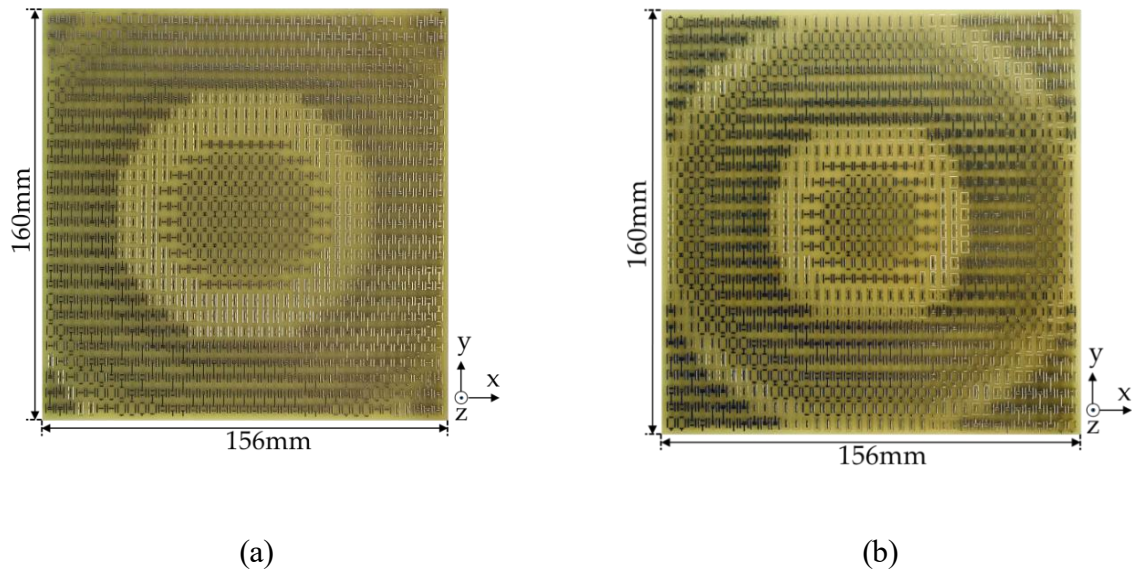


Figure 3.29. (a) Top view of the fabricated focusing lenses with 100 mm focal distance. (b) Top view of the fabricated focusing lenses with 60 mm focal distance.

3.4.1 Measurement Setup

Figure 3.3 shows the measurement setup; a focusing lens was fed by a half-wave dipole operating at 10 GHz at a specified focal distance and the focused beam from the array was captured by a standard horn antenna. The transmission coefficient (S_{21}) between the two antennas was measured using a vector network analyzer (Anritsu MS46122B, Anritsu Company, Morgan Hill, USA), and S_{21} values with and without the focusing lens were used to assess the focusing gain of the lens. For gain pattern measurements, the dipole antenna and the focusing lens were rotated horizontally in the same platform with a 1° step size and the measured pattern was compared with the simulation result. Distances between the dipole antenna and the focusing lens were maintained at the designed focal distances (100 and 60 mm).

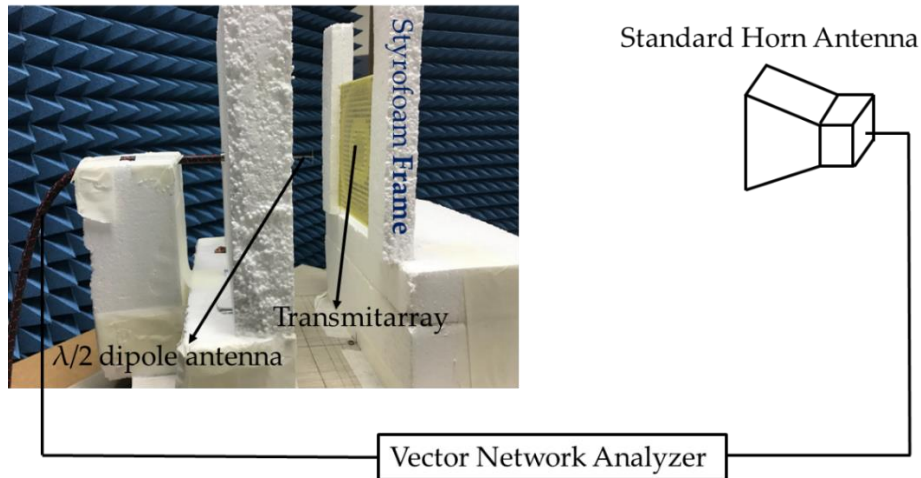


Figure 3.3. Setup for measuring the focusing gain of the focusing lens using a half-wave dipole antenna as the feeding source and a standard horn antenna. Both antennas were connected to a vector network analyzer.

3.4.2 Simulation and Measured Result

Figure 3.31 a,b demonstrates that the measured focusing gain at the boresight and sidelobe levels of both focusing lens correlated well with the simulation results at 10 GHz. The main beams at the boresight provided a focusing gain of 12.87 dB for $f = 100$ mm and 13.58 dB for $f = 60$ mm, which are approximately 0.5 ~ 0.7 dB lower than the simulated results of 13.47 and 14.09 dB, respectively. We attributed this difference to fabrication uncertainty, e.g., substrate property deviation in the focusing lens and the nonideal spherical wave radiation from the half-wave dipole antenna. However, a near 13 dB focusing gain level from a lossy FR4-based compact focusing lens ($5.1\lambda \times 5.2\lambda$) with a low f/D value of 0.39 is noteworthy. In Figure 3.31a, the discrepancy between both data in terms of the dip of the main lobe is noticeable and the reason should be slightly perturbed current distributions on the fabricated lens due to the manufacture-related factors. Focusing gain at the boresight according to frequency was also measured and compared with the simulation results, as shown in Figure 3.31 c, d.

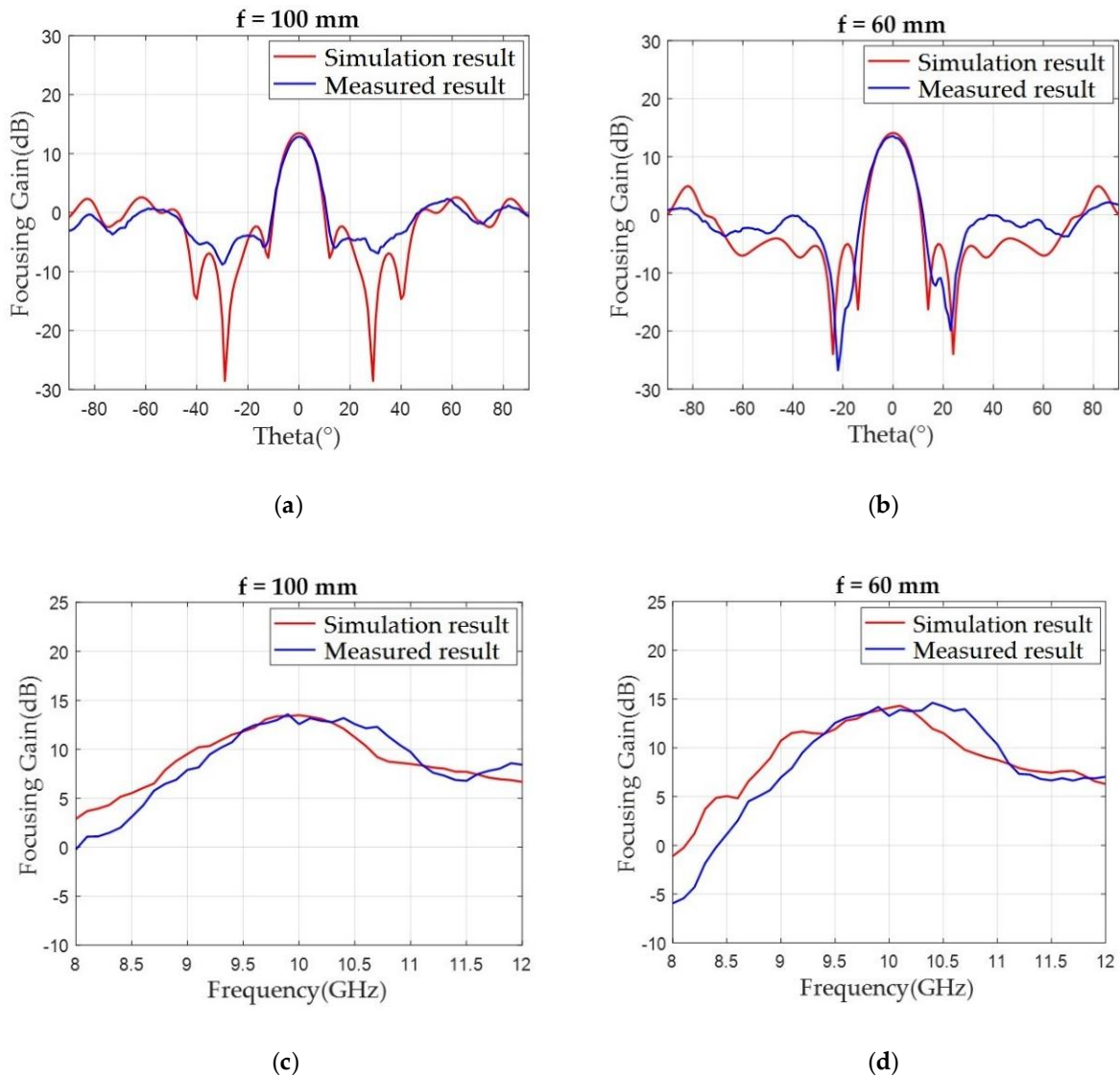


Figure 3.31. Simulated and measured and focusing gain patterns on the x - z plane as a function of theta at 10 GHz from the focusing lenses (a) with $f = 100$ mm and (b) with $f = 60$ mm. Simulated and measured focusing gain according to frequency from (c) $f = 100$ mm and (d) $f = 60$ mm.

3.4.3 Fractional Bandwidth Calculation

The measured data showed a slightly broader bandwidth compared to the simulated one with a wide 1 dB and 3 dB gain fractional bandwidth of near 13% and 18%, respectively. Figure 3.32(a) shows 1 dB fractional bandwidth calculation where f_c is the center frequency. In our case $f_c=10$

GHz. The other parameters f_H and f_L are the 1 dB higher and lower frequency from the center frequency, respectively.

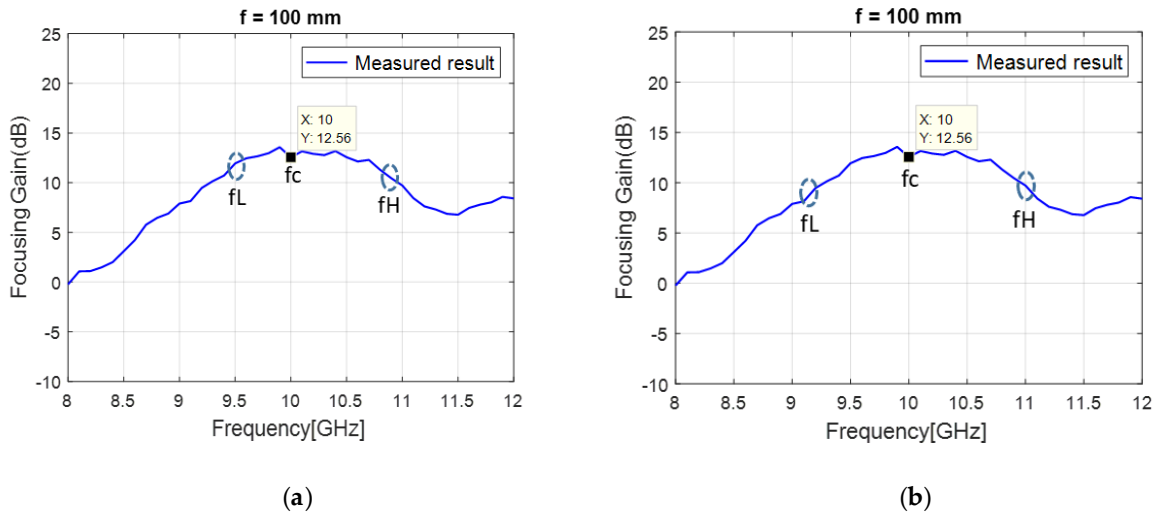


Figure 3.32. Fractional bandwidth for 100 mm focusing Lens. (a) 1 dB fractional bandwidth (b) 3 dB fractional bandwidth.

The 1 dB fractional bandwidth for the 100 mm focusing lens is shown as 13% using $FBW = (f_H - f_L)/f_c \times 100 = (10.8 - 9.5)/10 \times 100 = 13\%$. The 3 dB fractional bandwidth for the 100 mm focusing lens is shown as 18% using $FBW = (f_H - f_L)/f_c \times 100 = (11 - 9.2)/10 \times 100 = 18\%$ (see Figure 3.32(b)). Now for 60 mm focusing lens 1 dB and 3 dB focusing gain have been displayed in Figures 3.33.

The 1 dB fractional bandwidth for the 60 mm focusing lens is shown as 13% using $FBW = (f_H - f_L)/f_c \times 100 = (10.8 - 9.5)/10 \times 100 = 13\%$ (see Figure 3.33(a)).

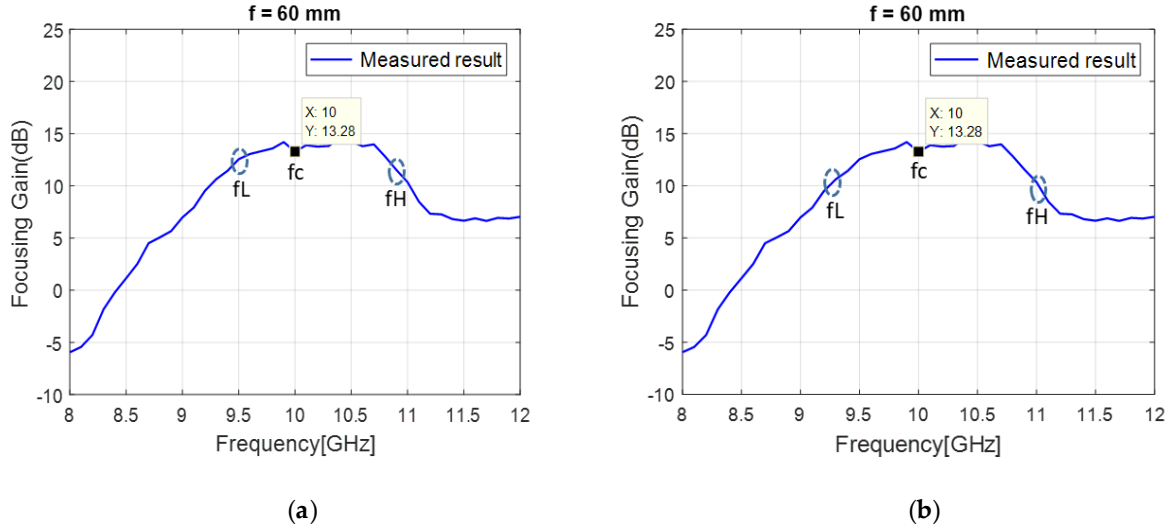


Figure 3.33. Fractional bandwidth for 60 mm focusing Lens. (a) 1 dB fractional bandwidth (b) 3 dB fractional bandwidth.

The 3 dB fractional bandwidth for the 60 mm focusing lens is shown as 17% using $FBW = (f_H - f_L)/f_c \times 100 = (11 - 9.3)/10 \times 100 = 17\%$ (see Figure 3.33(b)).

3.5 Discussion

We designed high transmission efficiency metasurface unit cells operating at 10 GHz in a double-layer FR4 with a thickness of 1.6 mm ($\lambda / 18.8$) for wide transmission phase coverage. The unit cells' physical structures were devised to implement perpendicularly directed surface electric and magnetic currents using the top and bottom metallic patterns and via drills. The proposed unit cells had three different topologies to control surface electric admittance (Y_{es}) and surface magnetic impedance (Z_{ms}) independently, providing compact (3.9×6.0 mm) 11 unit cells with an averaged -0.82 dB transmission loss and $-150^\circ \sim 150^\circ$ transmission phases. Performance comparison with the referenced designs is shown in Table 2 and it is important to note that the designed unit cells achieved the lowest transmission loss even in a lossy FR4 ($\tan \delta = 0.008$) substrate compared to the recently reported double-layer unit cells from Table 2.

To assess the efficiency of the proposed unit cells experimentally, we designed two focusing lenses with a size of 156×160 mm ($5.1\lambda \times 5.2\lambda$) to focus a radiated spherical beam in short focal distances ($f = 100$ and 60 mm). We expected the compact unit cell to maintain a low discretization

error with low f/D numbers ($f/D = 0.65$ and 0.39), which required steep phase variation in the focusing lens design. The fabricated focusing lenses boosted the half-wave dipole's gain more than 13 dB despite the short focal distances and achieved a wide 1 dB gain bandwidth of near 13%. Moreover, the focusing gain was increased by 0.7 dB with a focal distance change from 100 to 60 mm, demonstrating the low discretization error of the designed unit cells. From Table 2, the focusing gain levels of this work were lower within 3 dB compared to at least four times larger lenses in terms of center wavelength (λ), proving the higher focusing efficiency. Two slightly smaller lenses also showed 4~5 dB lower focusing gain values, and specifically, in [86], a compact ($3.5\lambda \times 3.5\lambda$) and a double-layer focusing lens with a low f/D of 0.29 showed focusing gain of 8.2 dB at 10 GHz. For a fair comparison, the aperture efficiencies using the measured focusing gain were calculated and a higher value of 6.88% from this work compared to 4.37% from [86] was shown. The higher efficiency from the designed lenses corresponds to the lower transmission loss from the proposed unit cells and manifests that higher spillover loss due to the broad radiation from the dipole antenna compared to the high gain patch antenna from [86] was also recovered. Moreover, the lens from [86] utilized narrow lateral dimensions for the phase coverage; it is thus subject to the narrow bandwidth (it was not reported).

Table 2. Performance comparison of the proposed focusing lenses with the referenced designs.

Ref.	Layer #	Freq. (GHz)	Loss tangent	Max. loss of unit cell (dB)	Lens size (mm × mm)	Thickness (mm)	Bandwidth (3 dB/1 dB)	f/D	Focusing gain (dB)
[90]	2	20	0.0014	-1.75	338 × 338 (22.5 λ × 22.5 λ)	1.575 ($\lambda / 9.5$)	-/5.9	1.24	14.9 ¹
[92]	2	28	0.0027	-1.63	165 × 165 (15.4 λ × 15.4 λ)	1.524 ($\lambda / 7.0$)	13.3/-	0.95	16.4
[88]	2	26.2	0.001	-1.56	171.6 × 171.6 (15 λ × 15 λ)	1.5 ($\lambda / 7.6$)	15.7/-	0.99	15.7 ¹
[87]	2	13	0.0037	-2.5	328 × 328 (14.2 λ × 14.2 λ)	0.762 ($\lambda / 30$)	3/-	0.8	11.5

[89]	2	10	0.005	-3	360 × 500 (12λ × 16.6λ)	2 (λ / 15)	6/-	0.3	7.65
[104]	3	10.2	0.004	-2.75	376.5 × 376.5 (12.8λ × 12.8λ)	1.1 (λ / 26.7)	9.8/-	0.8	14.4
[91]	2	6	-	-1.4	210 × 210 (4.2λ × 4.2λ)	2 (λ / 25)	15/-	0.8	9
[86]	2	10	0.001	-1.4	104 × 104 (3.46λ × 3.46λ)	3 (λ / 10)	-/-	0.29	8.2
This Work	2	10	0.008	-1.1	156 × 160 (5.1λ × 5.2λ)	1.6 (λ / 18.8)	20/10	0.65/ 0.39	12.87/ 13.58

¹Focusing gain was calculated using the simulated gain from the feeding antenna.

CHAPTER 4: RECONFIGURABLE INTELLIGENT SURFACE DESIGN FOR BEAM STEERING

In chapter 3, the detailed structure and performance of passive transmissive metasurface have been shown. To make the structure intelligent/reconfigurable, I incorporated PIN (positive-intrinsic-negative) diode and varactor diodes in topology-1 structure. In this chapter, I will present recent progress on reconfigurable metasurface and our design.

4.1 Reconfigurable Metasurface State of The Art

Nowadays, intelligent reconfigurable surfaces (IRS)/tunable metasurfaces have taken huge attention due to their beam manipulation capability in real-time. This tunable type metasurface can be used in the application of dynamic holography, imaging, beam shaping/steering, and focusing. However, in recent years, many attempts have been taken to achieve active control of metamaterial and metasurfaces by incorporating switchable meta-atom or active components such as microelectromechanical (MEMS), vanadium dioxide (VO₂), graphene, liquid crystal, GaAs switch, Schottky diode, PIN diode, and varactor diodes. A reconfigurable reflect-array based on MEMS has been presented for phase-shifting application [105]. This structure was fabricated on

SU-8 photo resistor substrate and provided discrete phase states of 0° , -90° , -180° , and -270° . In another work, an ultra-fast switching mechanism by utilizing an insulator to metal transition of VO_2 has been proposed [106]. This structure can manipulate wave front and provide four discontinuous reflection phase responses 0° , 90° , 180° , and 270° . Adopting the same technology, another structure has been presented with a phase scanning range of 0° to 59° [107]. Recently, graphene-based structures have taken attention due to their low loss plasmonic resonance and high operational frequency. A graphene patch embedded with Silicon Dioxide (SiO_2) has been revealed which can focus beam both in vertical (11.25°) and horizontal (0°) direction [108]. In another approach, reflect-array structure used graphene to achieve beam steering, shaping and broadband phase modulation [109]. This structure provides one-bit beam steering of 0° and 180° with an efficiency of -8 dB. One more active component, liquid crystal, has become a promising tool for beam steering application due to its low dielectric loss. In [110], a reflect-array with liquid crystal as RF substrate has been presented. The dielectric property of this structure can be varied upon the application of external voltage and can regulate beam focusing of 0° , 25° , and -10° . A similar liquid crystal-based structure has also been investigated in [111]. The beam steering angles of this structure are -6° , 0° , and 6° with gain of 25.1 dB.

In addition, investigation in diode-based structures is going on. A Schottky diode behaviour has been realized by using hybrid metal-semiconductor as substrate [112]. The doped semiconductor substrate was modified by the application of external voltage. This structure is a transmit-array and can deflect the beam at 17° , 59° , 118° and 137° . Alternatively, PIN diode has become a popular active component due to having some attractive features: low cost, low power consumption, and low driving voltage. The recent work on GaAs and PIN diode combination provides 1 bit switching in reflect-array [113]. Here, GaAs was used as substrate whereas ON/OFF condition of PIN diode generates two different phases of -180° and $+180^\circ$. Another PIN diode structure achieves beam steering angle of $180^\circ \pm 20^\circ$ [114]. Recently, varactor diodes have been actively investigated due to high-frequency operation and large-scale capacitance tuning. In [115], a varactor-based tunable reflect-array has been investigated. In this structure, MACOM varactor of model MAVR-011020-1411 has been used which can vary capacitance from 0.032 pF to 0.216 pF for 0-15 V bias voltage. This structure can switch beam focusing points in a range of $\pm 48^\circ$.

4.2 Problem Statement

Our main target is to achieve wide beam steering angles with high gain at 10 GHz. However, MEMS, Vanadium Dioxide, Graphene, Liquid Crystal, GaAs switch, and Schottky diode-based structure are bulky and heavy which make them less attractive for a compact device. On the other hand, these types of structures need complex fabrication technology and are difficult to achieve continuous phase scanning with a wide range. As an alternative, PIN diode can be seen as a promising component but for higher phase tuning range, it needs to connect many PIN diodes in complex structure [116]. The above-mentioned limitations were minimized by considering varactor diode as an active component for a wide range of beam scanning at high frequency [116]. Recently available microscale varactor diode and PIN diode made them perfect for integration in compact devices.

4.3 Unit Cell Design Process

We constructed a meta-atom or unit cell which comprises electric and magnetic dipole based on Huygens's principle. Although most of the tunable structures are reflection-based, our target is to make a transmit-array with highly transmissive unit cells by using fabrication-friendly PCB technology. We incorporated varactor diodes and PIN diode with magnetic and electric dipoles and connect them with a voltage source by using 0.2 mm width bias lines. The side view of the unit cell structure has been presented in Figure 4.1(a). However, the length of the PIN diode, $p_l = 0.63\text{mm}$, length of the varactor diode, $v_l = 1.5\text{mm}$, length of a RF blocking resistor, $r_l = 0.6\text{ mm}$ were fixed based on the commercial availability of those components. Electric dipole width $e_w = 0.9\text{ mm}$ and length of magnetic dipole arm $m_l = 3.61\text{ mm}$, fixed through optimization. The top view of the unit cell with active components and dimensions is presented in Figure 4.1 (b).

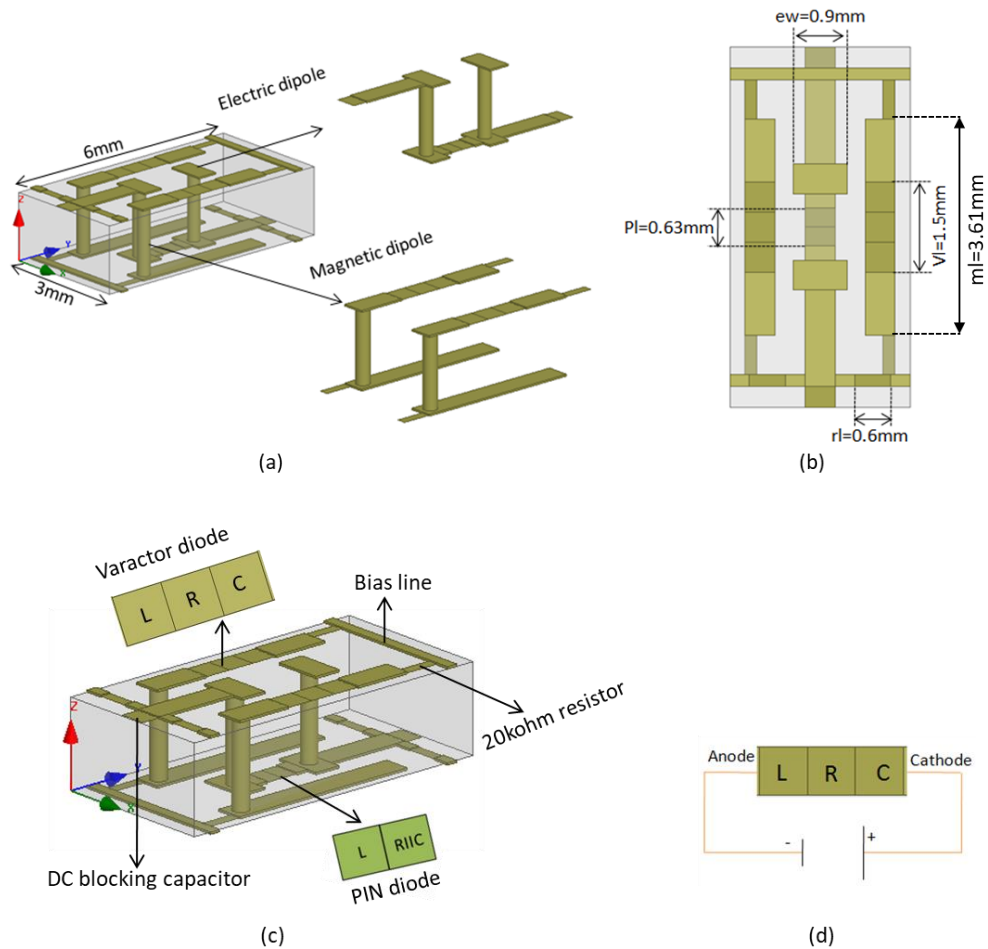


Figure 4.1 (a) Side view of electric and magnetic dipole in tunable unit cell. (b) Top view of unit cell. (c) Reconfigurable components PIN and varactor embedded with electric and magnetic dipole. Bias lines are for providing voltage across diodes. The 20 K Ω resistor and DC blocking Capacitor help to block RF and DC current, respectively. (d) Sketch of voltage application across diode.

The change of voltage will change the capacitance of the varactor and thus will vary excitation on the magnetic field of impinging electromagnetic wave. On the other hand, ON and OFF condition of PIN diode provides different excitation on the electric field. I used a single unit cell with average S_{21} of near -3 dB to cover -0° , $+90^\circ$, $+180^\circ$, and -90° phase at 10 GHz. The transmittance (S_{21}) will be made higher by carefully tuning surface electric admittance (Y_{es}) and surface magnetic impedance (Z_{ms}). The surface will be reflectionless when $Y_{es} = Z_{ms}$. However, In

HFSS, the varactor and PIN diode are realized by using lumped elements. In addition, the lumped elements were used for high resistors ($20\text{ K}\Omega$) on the bias line. The resistors were used to suppress unwanted RF current on the bias line. The DC current flow between adjacent unit cells was reduced by using a DC blocking capacitor ($1\mu\text{F}$) (see Figure 4.1 (c) and (d)). The reconfigurable unit cell transmission performance and phase profile are shown in Table 3.

Table 3. Geometric parameters simulated electric surface admittance (Y_{es}), magnetic surface impedance (Z_{ms}), transmission phases, and transmission loss of the tunable metasurface unit cells.

Varactor capacitance (pF)	PIN State (ON/OFF)	ml (mm)	ew (mm)	Im (Y_{es})	Im (Z_{ms})	Trans. phase ($^{\circ}$)	Trans. loss (dB)
1	ON			0.67	-1.03	-11	-5.6
0.3	OFF	3.61	0.9	-4.11	-0.93	100	-3.1
0.13	OFF			-4.68	-3.27	160	-3.9
0.11	ON			1.01	3.18	-89	-3.4

4.4 Lens Design and Expected Result

The required phases to form a lens were calculated using the Matlab program and unit cells will be placed accordingly. A $\lambda/2$ dipole antenna was used to feed the lens. The lens will not only increase the focusing gain but also tune the beam based on applied voltages. Our target is to achieve a continuous scanning range from -60° to $+60^{\circ}$ with high gain at every focusing point. In this way, we can be able to change the behavior of the radio environment between sender and receiver in real-time.

CHAPTER 5: CONCLUSION AND FUTURE WORK

5.1 Conclusion

Significant advances in two-layer transmissive metasurfaces were reported in this thesis. First, the invention of metamaterial and its development from a literature perspective was discussed. Then, the transition of three-dimensional and bulky metamaterials to two-dimensional and near-zero thickness sheets (metasurface) was illustrated. The metasurface can be designed both for reflection and transmission. Our contribution is in the area of transmissive metasurfaces which were discussed in detail throughout this thesis. However, in the first development of metasurface, the only electric dipole was used, which could not excite the magnetic field. As a consequence, full transmission and whole phase coverage could not be achieved simultaneously. This limitation was overcome by introducing Huygens' metasurface, which comprises both electric and magnetic dipoles and can simultaneously excite electric and magnetic currents. Firstly, Huygens' metasurface of different layers and comparison of their transmission performance was illustrated. Later, a detailed design procedure of Huygens' metasurface as our contribution was presented. Next, highly efficient transmissive unit cells based on Huygens' principle were designed. Then, thorough search, the recent development in transmission metasurfaces was communicated. Next, a mathematical representation and analysis of generalized sheet transition condition (GSTC) and Huygens' principle were presented. After that, the analysis and implementation of the metasurface was performed by full-wave simulation software, HFSS. Moreover, the focusing performance of the fabricated lens was verified with simulation results. Finally, the superiority of this structure was compared with a wide range of relevant states of the arts.

This research was extended to a reconfigurable metasurface by using the above-mentioned highly efficient Huygens' metasurface unit cells. In this case, PIN and varactor diodes as tunable components were embedded. By changing the state of the PIN diode from ON to OFF and by varying capacitance of the varactor diode, four-phase states were achieved with good transmission performance. The target was to regulate the beam focusing point from $+60^\circ$ to -60° with high gain. Finally, as an expectation, the high gain focusing lens with a low f/D based on the FR4-based high-

efficiency double-layer unit cells can be utilized for low-profile beam-forming antenna systems in 5G and millimeter-wave communications.

5.2 Proposal for future works

Throughout this thesis, we demonstrated the principle and design criteria of Huygens' metasurface unit cell with good transmission performance. We presented different techniques adopted by researchers to reduce the thickness of the metasurface in the chapter 2. In addition, in section 3.1 we demonstrated layer reduction techniques through a literature review. The complete design procedure of the lens was developed in chapter 3 with an explanation. However, based on the design in chapter 3, we designed reconfigurable metasurface unit cells by incorporating PIN and varactor diodes. The design procedure of a reconfigurable metasurface unit cell was depicted in chapter 4. In the future, we will expand our research to use the surface for 5G and 6G applications. We can make the reconfigurable surface more intelligent, real-time, and practical by deploying a machine learning algorithm. In this case, a sensor will collect data about the location of the mobile station (MS). Then, the algorithm will be trained for generating the required voltage combination to regulate the beam towards the mobile location. When the mobile location is changed, the sensor will sense and urge the algorithm to generate the newly required voltage combination. A Field Programmable Gate Array (FPGA) will be used to provide the necessary voltage to the structure.

References:

- [1] Abdelrahman AH, Elsherbeni A Z and Yang F 2014 High-gain and broadband transmitarray antenna using triple-layer spiral dipole elements *IEEE Trans. Antennas Propag.* **13** 1288
- [2] Erdil E, Topalli K, Esmaeilzad N S, Zorlu O, Kulah H and Civi O A 2015 Reconfigurable nested ring-split ring transmitarray unit cell employing the element rotation method by microfluidics *IEEE Trans. Antennas Propag.* **63** 1164
- [3] R. W. Ziolkowski, "Metamaterials: The early years in the USA," *EPJ Appl. Metamat.*, vol. 1, p. 5, Jul. 2014
- [4] J. S. Derov, R. Hammond, and I. J. Youngs, "The history of the early years of metamaterials in USA and UK defense agencies," *J. Opt.*, vol. 19, no. 8, Aug. 2017, Art. no. 084002

- [5] J. B. Pendry, "Negative refraction makes a perfect lens," *Phys. Rev. Lett.*, vol. 85, no. 18, pp. 3966–3969, Jul. 2002.
- [6] J. B. Pendry, "Controlling electromagnetic fields," *Science*, vol. 312, no. 5781, pp. 1780–1782, Jun. 2006
- [7] A. Alù and N. Engheta, "Achieving transparency with plasmonic and metamaterial coatings," *Phys. Rev. E, Stat. Phys. Plasmas Fluids Relat. Interdiscip. Top.*, vol. 72, no. 1, Jul. 2005, Art. no. 016623.
- [8] A. Grbic and G. V. Eleftheriades, "Overcoming the diffraction limit with a planar left-handed transmission-line lens," *Phys. Rev. Lett.*, vol. 92, no. 11, Mar. 2004, Art. no. 117403.
- [9] A. K. Iyer and G. V. Eleftheriades, "Free-space imaging beyond the diffraction limit using a Veselago-Pendry transmission-line metamaterial superlens," *IEEE Trans. Antennas Propag.*, vol. 57, no. 6, pp. 1720–1727, Jun. 2009.
- [10] D. Schurig et al., "Metamaterial electromagnetic cloak at microwave frequencies," *Science*, vol. 314, no. 5801, pp. 977–980, Nov. 2006.
- [11] D. Rainwater, A. Kerkhoff, K. Melin, J. C. Soric, G. Moreno, and A. Alù, "Experimental verification of three-dimensional plasmonic cloaking in free-space," *New J. Phys.*, vol. 14, no. 1, Jan. 2012, Art. no. 013054.
- [12] F. Falcone, T. Lopetegi, J. Baena, R. Marques, F. Martín, and M. Sorolla, "Effective negative- ϵ stopband microstrip lines based on complementary split ring resonators," *IEEE Microw. Wireless Compon. Lett.*, vol. 14, no. 6, pp. 280–282, Jun. 2004
- [13] N. Engheta, A. Salandrino, and A. Alù, "Circuit elements at optical frequencies: Nanoinductors, nanocapacitors, and nanoresistors," *Phys. Rev. Lett.*, vol. 95, no. 9, pp. 095504-1–095504-4, Aug. 2005.
- [14] N. Engheta, "Circuits with light at nanoscales: Optical nanocircuits inspired by metamaterials," *Science*, vol. 317, no. 5845, pp. 1698–1702, Sep. 2007.
- [15] P.-S. Kildal, "Artificially soft and hard surfaces in electromagnetics," *IEEE Trans. Antennas Propag.*, vol. 38, no. 10, pp. 1537–1544, 1990
- [16] S. Linden, "Magnetic response of metamaterials at 100 terahertz," *Science*, vol. 306, no. 5700, pp. 1351–1353, Nov. 2004.
- [17] H. Mosallaei and K. Sarabandi, "Antenna miniaturization and bandwidth enhancement using a reactive impedance substrate," *IEEE Trans. Antennas Propag.*, vol. 52, no. 9, pp. 2403–2414, Sep. 2004
- [18] D. Sievenpiper, J. Schaffner, H. Song, R. Loo, and G. Tangonan, "Twodimensional beam steering using an electrically tunable impedance surface," *IEEE Trans. Antennas Propag.*, vol. 51, no. 10, pp. 2713–2722, Oct. 2003.
- [19] X. Ni, N. K. Emani, A. V. Kildishev, A. Boltasseva, and V. M. Shalaev, "Broadband light bending with plasmonic

nanoantennas,” *Science*, vol. 335, no. 6067, p. 427, Jan. 2012.

[20] R. Bansal, “Bending snell’s laws [AP-S turnstile],” *IEEE Antennas Propag. Mag.*, vol. 53, no. 5, pp. 146–147, Oct. 2011.

[21] Z. Bomzon, G. Biener, V. Kleiner, and E. Hasman, “Space-variant Pancharatnam-Berry phase optical elements with computer-generated subwavelength gratings,” *Opt. Lett.*, vol. 27, no. 13, pp. 1141–1143, Jul. 2002.

[22] E. Silberstein, P. Lalanne, J.-P. Hugonin, and Q. Cao, “Use of grating theories in integrated optics,” *J. Opt. Soc. Amer. A, Opt. Image Sci.*, vol. 18, no. 11, p. 2865, Nov. 2001

[23] P. Lalanne and P. Chavel, “Metalenses at visible wavelengths: Past, present, perspectives,” *Laser Photon. Rev.*, vol. 11, no. 3, May 2017, Art. no. 1600295

[24] H.-H. Hsiao, C. H. Chu, and D. P. Tsai, “Fundamentals and applications of metasurfaces,” *Small Methods*, vol. 1, no. 4, p. 1600064, 2017. 3, 4

[25] Y. Zhao and A. Alu, “Tailoring the dispersion of plasmonic nanorods to realize broadband optical meta-waveplates,” *Nano letters*, vol. 13, no. 3, pp. 1086–1091, 2013. 3

[26] Y. Zhao and A. Alù, “Manipulating light polarization with ultrathin plasmonic metasurfaces,” *Physical Review B*, vol. 84, no. 20, p. 205428, 2011. 3

[27] D. Lin, P. Fan, E. Hasman, and M. L. Brongersma, “Dielectric gradient metasurface optical elements,” *science*, vol. 345, no. 6194, pp. 298–302, 2014. 3, 5

[28] E. Schonbrun, K. Seo, and K. B. Crozier, “Reconfigurable imaging systems using elliptical nanowires,” *Nano letters*, vol. 11, no. 10, pp. 4299–4303, 2011. 3

[29] A. Arbabi, Y. Horie, M. Bagheri, and A. Faraon, “Dielectric metasurfaces for complete control of phase and polarization with subwavelength spatial resolution and high transmission,” *Nature nanotechnology*, vol. 10, no. 11, p. 937, 2015. 3

[30] Y. F. Yu, A. Y. Zhu, R. Paniagua-Domínguez, Y. H. Fu, B. Luk’yanchuk, and A. I. Kuznetsov, “High-transmission dielectric metasurface with 2... phase control at visible wavelengths,” *Laser & Photonics Reviews*, vol. 9, no. 4, pp. 412–418, 2015. 3, 7

[31] L. Wang, S. Kruk, H. Tang, T. Li, I. Kravchenko, D. N. Neshev, and Y. S. Kivshar, “Grayscale transparent metasurface holograms,” *Optica*, vol. 3, no. 12, pp. 1504–1505, 2016. 3, 7

[32] K. E. Chong, L. Wang, I. Staude, A. R. James, J. Dominguez, S. Liu, G. S. Subramania, M. Decker, D. N. Neshev, I. Brener, et al., “Efficient polarization-insensitive complex wavefront control using Huygens’ metasurfaces

based on dielectric resonant meta-atoms,” *Acs Photonics*, vol. 3, no. 4, pp. 514–519, 2016. 3, 7

[33] J. B. Mueller, K. Leosson, and F. Capasso, “Ultracompact metasurface in-line polarimeter,” *Optica*, vol. 3, no. 1, pp. 42–47, 2016. 3

[34] F. Ding, Y. Chen, and S. I. Bozhevolnyi, “Metasurface-based polarimeters,” *Applied Sciences*, vol. 8, no. 4, p. 594, 2018. 3

[35] M. I. Shalaev, J. Sun, A. Tsukernik, A. Pandey, K. Nikolskiy, and N. M. Litchinitser, “High efficiency all-dielectric metasurfaces for ultracompact beam manipulation in transmission mode,” *Nano letters*, vol. 15, no. 9, pp. 6261–6266, 2015. 3, 6, 7

[36] C. Huygens, *Traité de la lumière*. Pieter van der Aa, 1690. 3

[37] <https://www.theses.fr/2019BORD0415.pdf>

[38] C. Huygens, *Traité de la Lumière*. Leyden, 1690. Translated into English by S. P. Thompson, London, 1912, reprinted by The University of Chicago Press

[39] A. Love, “The integration of the equations of propagation of electric waves. series a,” *Philosophical Trans. of the Royal Society of London*, vol. 197, pp. 1–45, 1901.

[40] S. Schelkunoff, “Some equivalence theorems of electromagnetics and their application to radiation problems,” *Bell Syst. Tech. J.*, vol. 15, no. 1, 1936.

[41] C. A. Balanis, *Antenna theory: analysis and design*. John Wiley & Sons, 2012.

[42] R. F. Harrington, *Time-Harmonic Electromagnetic Fields*. McGraw-Hill, 1961.

[43] M. Selvanayagam and G. V. Eleftheriades, “Discontinuous electromagnetic fields using orthogonal electric and magnetic currents for wavefront manipulation,” *Optics Express*, vol. 21, no. 12, pp. 14 409–14 429, Jun 2013. [Online]. Available: <http://www.opticsexpress.org/abstract.cfm?URI=oe-21-12-14409>

[44] C. Pfeiffer and A. Grbic, “Metamaterial Huygens surfaces: Tailoring wave fronts with reflectionless sheets,” *Physical Review Letters*, vol. 110, p. 197401, 2013

[45] H. A. Wheeler, “Simple relations derived from a phased-array antenna made of an infinite current sheet,” *IEEE Transactions on Antennas and Propagation*, vol. 13, p. 506–514, 1965.

[46] E. F. Kuester, M. A. Mohamed, M. Piket-May, and C. L. Holloway, “Averaged transition conditions for electromagnetic fields at a metafilm,” *IEEE Trans. on Antennas and Propag.*, vol. 51, no. 10, pp. 2641–2651, October 2003

- [47] S. Tretyakov, *Analytical Modelling in Applied Electromagnetics*. Artech House, 2003.
- [48] M. Selvanayagam and G. V. Eleftheriades, "Circuit modelling of Huygens surfaces," *IEEE Antennas and Wirel. Propag. Lett.*, vol. 12, pp. 1642-1645, 2013.
- [49] Q. Wu, F.-Y. Meng, M. Wu, J. Wu, and L.-W. Li, "Research on the negative permittivity effect of the thin wires array in left-handed material by transmission line theory," *PIERS Online*, vol. 1, p. 196200, 2005.
- [50] D. M. Pozar, S. D. Targonski, and H. D. Syrigos, "Design of millimeter wave microstrip reflectarrays," *IEEE Transactions on Antennas and Propagation*, vol. 45, pp. 287-296, 1997.
- [51] H. A. Wheeler, "Simple relations derived from a phased-array antenna made of an infinite current sheet," *IEEE Transactions on Antennas and Propagation*, vol. 13, p. 506-514, 1965.
- [52] E. F. Kuester, C. Holloway, and M. Mohamed, "A generalized sheet transition condition model for a metafilm partially embedded in an interface," *APSURSI*, vol. 1, no. 4, pp. 11-17, July 2010.
- [53] C. Holloway, M. Mohamed, E. F. Kuester, and A. Dienstfrey, "Reflection and transmission properties of a metafilm: with an application to a controllable surface composed of resonant particles," *IEEE Trans. on Electromagn. Compat.*, vol. 47, no. 4, pp. 853-865, November 2005.
- [54] S. Kim, E. Kuester, C. Holloway, A. Scher, and J. Baker-Jarvis, "Boundary effects on the determination of metamaterial parameters from normal incidence reflection and transmission measurements," *IEEE Trans. on Antennas and Propag.*, vol. 59, no. 6, pp. 2226-2240, June 2011.
- [55] C. Holloway, E. Kuester, and A. Dienstfrey, "Characterizing metasurfaces/metafilms: The connection between surface susceptibilities and effective material properties," *IEEE Antennas and Wirel. Propag. Lett.*, vol. 10, pp. 1507-1511, 2011.
- [56] Yu, N.; Genevet, P.; Kats, M.A.; Aieta, F.; Tetienne, J.-P.; Capasso, F.; Gaburro, Z. Light Propagation with Phase Discontinuities: Generalized Laws of Reflection and Refraction. *Science* 2011, 334, 333-337.
- [57] Pfeiffer, C.; Grbic, A. Metamaterial Huygens' surfaces: Tailoring wave fronts with reflectionless sheets. *Phys. Rev. Lett.* 2013, 110, 197401.
- [58] Yu, N.; Genevet, P.; Aieta, F.; Kats, M.A.; Blanchard, R.; Aoust, G.; Tetienne, J.-P.; Gaburro, Z.; Capasso, F. Flat Optics: Controlling Wavefronts with Optical Antenna Metasurfaces. *IEEE J. Sel. Top. Quantum Electron.* 2013, 19, 4700423.
- [59] Liu, S.; Cheng, Q.; Xu, Q.; Wang, T.Q.; Du, L.L.; Luan, K.; Xu, Y.H.; Bao, D.; Fu, X.J.; Han, J.G.; et al. Free-Standing Metasurfaces for High-Efficiency Transmitarrays for Controlling Terahertz Waves. *Adv. Opt. Mater.*

2016, 4, 384–390.

[60] Pfeiffer, C.; Emani, N.K.; Shaltout, A.M.; Boltasseva, A.; Shalaev, V.M.; Grbic, A. Efficient Light Bending with Isotropic Metamaterial Huygens' Surfaces. *Nano Lett.* 2014, 14, 2491–2497.

[61] Pfeiffer, C.; Grbic, A. Bianisotropic Metasurfaces for Optimal Polarization Control: Analysis and Synthesis. *Phys. Rev. Appl.* 2014, 2, 044011.

[62] Pfeiffer, C.; Grbic, A. Cascaded metasurfaces for complete phase and polarization control. *Appl. Phys. Lett.* 2013, 102, 231116.

[63] Pfeiffer, C.; Zhang, C.; Ray, V.; Guo, L.J.; Grbic, A. High Performance Bianisotropic Metasurfaces: Asymmetric Transmission of Light. *Phys. Rev. Lett.* 2014, 113, 023902.

[64] Jia, S.L.; Wan, X.; Bao, D.; Zhao, Y.J.; Cui, T.J. Independent controls of orthogonally polarized transmitted waves using a Huygens metasurface. *Laser Photonics Rev.* 2015, 9, 545–553.

[65] Pfeiffer, C.; Grbic, A. Controlling Vector Bessel Beams with Metasurfaces. *Phys. Rev. Appl.* 2014, 2, 044012.

[66] Pfeiffer, C.; Zhang, C.; Ray, V.; Guo, L.J.; Grbic, A. Polarization rotation with ultra-thin bianisotropic metasurfaces. *Optica* 2016, 3, 427.

[67] Qin, F.; Wan, L.; Li, L.; Zhang, H.; Wei, G.; Gao, S. A Transmission Metasurface for Generating OAM Beams. *IEEE Antennas Wirel. Propag. Lett.* 2018, 17, 1793–1796.

[68] Jiang, S.; Chen, C.; Zhang, H.; Chen, W. Achromatic electromagnetic metasurface for generating a vortex wave with orbital angular momentum (OAM). *Opt. Express* 2018, 26, 6466.

[69] Chen, M.L.N.; Jiang, L.J.; Sha, W.E.I. Ultrathin Complementary Metasurface for Orbital Angular Momentum Generation at Microwave Frequencies. *IEEE Trans. Antennas Propag.* 2017, 65, 396–400.

[70] Zhang, K.; Wang, Y.; Yuan, Y.; Burokur, S.N. A Review of Orbital Angular Momentum Vortex Beams Generation: From Traditional Methods to Metasurfaces. *Appl. Sci.* 2020, 10, 1015.

[71] Holloway, C.L.; Kuester, E.F.; Gordon, J.A.; O'Hara, J.; Booth, J.; Smith, D.R. An Overview of the Theory and Applications of Metasurfaces: The Two-Dimensional Equivalents of Metamaterials. *IEEE Antennas Propag. Mag.* 2012, 54, 10–35.

[72] Kildishev, A.V.; Boltasseva, A.; Shalaev, V.M. Planar Photonics with Metasurfaces. *Science* 2013, 339, 1232009.

[73] Chen, H.-T.; Taylor, A.J.; Yu, N. A review of metasurfaces: Physics and applications. *Rep. Prog. Phys.* 2016, 79, 076401.

- [74] Glybovski, S.B.; Tretyakov, S.A.; Belov, P.A.; Kivshar, Y.S.; Simovski, C.R. Metasurfaces: From microwaves to visible. *Phys. Rep.* 2016, 634, 1–72.
- [75] He, Q.; Sun, S.; Xiao, S.; Zhou, L. High-Efficiency Metasurfaces: Principles, Realizations, and Applications. *Adv. Opt. Mater.* 2018, 6, 1800415.
- [76] Azad, A.K.; Efimov, A.V.; Ghosh, S.; Singleton, J.; Taylor, A.J.; Chen, H.-T. Ultra-thin metasurface microwave flat lens for broadband applications. *Appl. Phys. Lett.* 2017, 110, 224101.
- [77] Lin, D.; Holsteen, A.L.; Maguid, E.; Fan, P.; Kik, P.G.; Hasman, E.; Brongersma, M.L. Polarization independent metasurface lens employing the Pancharatnam-Berry phase. *Opt. Express* 2018, 26, 24835.
- [78] Ho, J.S.; Qiu, B.; Tanabe, Y.; Yeh, A.J.; Fan, S.; Poon, A.S.Y. Planar immersion lens with metasurfaces. *Phys. Rev. B* 2015, 91, 125145.
- [79] Epstein, A.; Eleftheriades, G.V. Arbitrary Antenna Arrays Without Feed Networks Based on Cavity-Excited Omega-Bianisotropic Metasurfaces. *IEEE Trans. Antennas Propag.* 2017, 65, 1749–1756. *Sensors* 2020, 20, 6142
15 of 16
- [80] Epstein, A.; Wong, J.P.; Eleftheriades, G.V. Cavity-excited Huygens' metasurface antennas for near-unity aperture illumination efficiency from arbitrarily large apertures. *Nat. Commun.* 2016, 7, 1–10.
- [81] Chen, M.; Epstein, A.; Eleftheriades, G.V. Design and Experimental Verification of a Passive Huygens' Metasurface Lens for Gain Enhancement of Frequency-Scanning Slotted-Waveguide Antennas. *IEEE Trans. Antennas Propag.* 2019, 67, 4678–4692.
- [82] Olk, A.E.; Powell, D.A. Huygens Metasurface Lens for W-Band Switched Beam Antenna Applications. *IEEE Open J. Antennas Propag.* 2020, 1, 290–299.
- [83] Wang, Z.; Ding, X.; Zhang, K.; Ratni, B.; Burokur, S.N.; Gu, X.; Wu, Q. Huygens Metasurface Holograms with the Modulation of Focal Energy Distribution. *Adv. Opt. Mater.* 2018, 6, 1800121.
- [84] Wan, W.; Gao, J.; Yang, X. Metasurface Holograms for Holographic Imaging. *Adv. Opt. Mater.* 2017, 5, 1700541.
- [85] Liu, G.; Wang, H.; Jiang, J.; Xue, F.; Yi, M. A High-Efficiency Transmitarray Antenna Using Double Split Ring Slot Elements. *IEEE Antennas Wirel. Propag. Lett.* 2015, 14, 1415–1418.
- [86] Li, H.; Wang, G.; Liang, J.; Gao, X.; Hou, H.; Jia, X. Single-Layer Focusing Gradient Metasurface for Ultrathin Planar Lens Antenna Application. *IEEE Trans. Antennas Propag.* 2017, 65, 1452–1457.
- [87] Wu, L.W.; Ma, H.F.; Gou, Y.; Wu, R.Y.; Wang, Z.X.; Wang, M.; Gao, X.; Cui, T.J. High-transmission ultrathin huygens' metasurface with 360 phase control by using double-layer transmitarray elements. *Phys. Rev. Appl.* 2019,

12, 024012.

[88] Xue, C.; Lou, Q.; Chen, Z.N. Broadband Double-Layered Huygens' Metasurface Lens Antenna for 5G Millimeter-Wave Systems. *IEEE Trans. Antennas Propag.* 2020, 68, 1468–1476.

[89] Kou, N.; Yu, S.; Ding, Z.; Zhang, Z. One-Dimensional Beam Scanning Transmitarray Lens Antenna Fed by Microstrip Linear Array. *IEEE Access* 2019, 7, 90731–90740.

[90] An, W.; Xu, S.; Yang, F.; Li, M. A Double-Layer Transmitarray Antenna Using Malta Crosses with Vias. *IEEE Trans. Antennas Propag.* 2016, 64, 1120–1125.

[91] Chen, Y.; Chen, L.; Yu, J.-F.; Shi, X.-W. A C-Band Flat Lens Antenna with Double-Ring Slot Elements. *IEEE Antennas Wirel. Propag. Lett.* 2013, 12, 341–344.

[92] Xue, C.; Sun, J.; Niu, L.; Lou, Q. Ultrathin Dual-Polarized Huygens' Metasurface: Design and Application. *Ann. Phys.* 2020, 532, 2000151.

[93] Wong, J.P.; Selvanayagam, M.; Eleftheriades, G.V. Design of unit cells and demonstration of methods for synthesizing Huygens metasurfaces. *Photonics Nanostruct.-Fundam. Appl.* 2014, 12, 360–375.

[94] Wong, J.P.S.; Selvanayagam, M.; Eleftheriades, G.V. Polarization Considerations for Scalar Huygens Metasurfaces and Characterization for 2-D Refraction. *IEEE Trans. Microw. Theory Tech.* 2015, 63, 913–924.

[95] Wan, X.; Jia, S.L.; Cui, T.J.; Zhao, Y.J. Independent modulations of the transmission amplitudes and phases by using Huygens metasurfaces. *Sci. Rep.* 2016, 6, 25639.

[96] Epstein, A.; Eleftheriades, G.V. Arbitrary power-conserving field transformations with passive lossless omega-type bianisotropic metasurfaces. *IEEE Trans. Antennas Propag.* 2016, 64, 3880–3895.

[97] Chen, M.; Abdo-Sánchez, E.; Epstein, A.; Eleftheriades, G.V. Theory, design, and experimental verification of a reflectionless bianisotropic Huygens' metasurface for wide-angle refraction. *Phys. Rev. B* 2018, 97, 125433.

[98] Jouanlanne, C.; Clemente, A.; Huchard, M.; Keignart, J.; Barbier, C.; Le Nadan, T.; Petit, L. Wideband Linearly Polarized Transmitarray Antenna for 60 GHz Backhauling. *IEEE Trans. Antennas Propag.* 2017, 65, 1440–1445.

[99] Luo, Q.; Gao, S.; Sobhy, M.; Yang, X. Wideband Transmitarray with Reduced Profile. *IEEE Antennas Wirel. Propag. Lett.* 2018, 17, 450–453.

[100] Epstein, A.; Eleftheriades, G.V. Huygens' metasurfaces via the equivalence principle: Design and applications. *J. Opt. Soc. Am. B* 2016, 33, A31.

[101] Al-Joumayly, M.A.; Behdad, N. Wideband Planar Microwave Lenses Using Sub-Wavelength Spatial Phase

Shifters. *IEEE Trans. Antennas Propag.* 2011, 59, 4542–4552. *Sensors* 2020, 20, 6142 16 of 16

[102] Li, M.; Behdad, N. Wideband True-Time-Delay Microwave Lenses Based on Metallo-Dielectric and All-Dielectric Lowpass Frequency Selective Surfaces. *IEEE Trans. Antennas Propag.* 2013, 61, 4109–4119.

[103] Oh, J. Millimeter-Wave Thin Lens Employing Mixed-Order Elliptic Filter Arrays. *IEEE Trans. Antennas Propag.* 2016, 64, 3222–3227.

[104] Wang, Z.X.; Wu, J.W.; Wan, X.; Wu, L.W.; Xiao, Q.; Cheng, Q.; Cui, T.J. Broadband and ultrathin Huygens metasurface with high transmittance. *J. Phys. D Appl. Phys.* 2020, 53, 455102.

[105] Zhou Du; Tamminen, A.; Ala-Laurinaho, J.; Säily, J.; Rantakari, P.; Luukanen, A.; Räisänen, A.V. Design and Optimization of Reconfigurable Reflectarray Element with MEMS Phase Shifter. In Proceedings of the 2013 7th European Conference on Antennas and Propagation (EuCAP); April 2013; pp. 2422–2426.

[106] Shabanpour, J.; Beyraghi, S.; Cheldavi, A. Ultrafast Reprogrammable Multifunctional Vanadium-Dioxide-Assisted Metasurface for Dynamic THz Wavefront Engineering. *Scientific Reports* 2020, 10, 8950, doi:10.1038/s41598-020-65533-9.

[107] Hashemi, M.R.M.; Yang, S.-H.; Wang, T.; Sepúlveda, N.; Jarrahi, M. Electronically-Controlled Beam-Steering through Vanadium Dioxide Metasurfaces. *Scientific Reports* 2016, 6, 35439, doi:10.1038/srep35439.

[108] Sahandabadi, S.; Makki, S.V.A.-D.; Alirezaee, and S. Design of a Reflectarray Antenna Using Graphene and Epsilon-Near-Zero Metamaterials in Terahertz Band. *Progress In Electromagnetics Research Letters* 2020, 89, 113–119, doi:10.2528/PIERL19120601.

[109] Tamagnone, M.; Capdevila, S.; Lombardo, A.; Wu, J.; Centeno, A.; Zurutuza, A.; Ionescu, A.M.; Ferrari, A.C.; Mosig, J.R. Graphene Reflectarray Metasurface for Terahertz Beam Steering and Phase Modulation. arXiv:1806.02202 [cond-mat, physics:physics] 2018

[110] Moessinger, A.; Dieter, S.; Menzel, W.; Mueller, S.; Jakoby, R. Realization and Characterization of a 77 GHz Reconfigurable Liquid Crystal Reflectarray. In Proceedings of the 2009 13th International Symposium on Antenna Technology and Applied Electromagnetics and the Canadian Radio Science Meeting; February 2009; pp. 1–4.

[111] Bildik, S.; Dieter, S.; Fritsch, C.; Menzel, W.; Jakoby, R. Reconfigurable Folded Reflectarray Antenna Based Upon Liquid Crystal Technology. *IEEE Transactions on Antennas and Propagation* 2015, 63, 122–132, doi:10.1109/TAP.2014.2367491.

[112] Su, X.; Ouyang, C.; Xu, N.; Cao, W.; Wei, X.; Song, G.; Gu, J.; Tian, Z.; O'Hara, J.F.; Han, J.; et al. Active Metasurface Terahertz Deflector with Phase Discontinuities. *Opt. Express, OE* 2015, 23, 27152–27158, doi:10.1364/OE.23.027152.

- [113] Pan, X.; Yang, F.; Xu, S.; Li, M. Mode Analysis of 1-Bit Reflectarray Element Using p-i-n Diode at W-Band. In Proceedings of the 2017 IEEE International Symposium on Antennas and Propagation USNC/URSI National Radio Science Meeting; July 2017; pp. 2055–2056.
- [114]. Zhang, Z.; Lan, F.; Mazumder, P.; Wang, L.; Zeng, H.; Yang, Z.; Song, T.; Yin, J.; Shi, Z.; Xiao, B. Electrically Discretized Sub-Terahertz Phase Shifter Based on Novel Independent Phase Delay Meta-Atoms. In Proceedings of the 2019 Photonics Electromagnetics Research Symposium - Fall (PIERS - Fall); December 2019; pp. 3232–3234.
- [115] Rotshild, D.; Rahamim, E.; Abramovich, A. Innovative Reconfigurable Metasurface 2-D Beam-Steerable Reflector for 5G Wireless Communication. *Electronics* 2020, 9, 1191, doi:10.3390/electronics9081191.
- [116] Yang, X.; Xu, S.; Yang, F.; Li, M. A Novel 2-Bit Reconfigurable Reflectarray Element for Both Linear and Circular Polarizations. In Proceedings of the 2017 IEEE International Symposium on Antennas and Propagation USNC/URSI National Radio Science Meeting; July 2017; pp. 2083–2084.